



---

# Scalable Characterisation of Entanglement on Physical Quantum Computers

---

*Author:*

Haiyue Kang  
*Supervised by:*

Lloyd Hollenberg  
Gary Mooney

Master of Science (Physics)  
December 2023

School of Physics  
Faculty of Science  
**THE UNIVERSITY OF MELBOURNE**

A thesis submitted in partial fulfilment for the  
degree of Master of Science (Physics)

# Abstract

Aimed at benchmarking the capabilities of near-term Noisy Intermediate-Scale Quantum (NISQ) devices, this thesis focuses on approaches to characterising the entanglement of large-scale graph states prepared on those devices. In this work, using a highly scalable method, we verify the generation of bipartite entanglement on all nearest-neighbour qubits from a record-breaking 414-qubit graph state. We also study the method of randomised Pauli-string observables in fidelity estimation and demonstrate entanglement of up to 14 qubits, and develop a new tool of energy estimation for measuring entanglement and demonstrate it in cases of up to 127 qubits. Furthermore, we achieve a doubling in the coherence time of the graph state using entanglement preservation protocol. Finally, we realize the preservation of entanglement after at least 11 teleporting jumps between physical qubits.

# Statement of Contribution and Originality

This is to certify that the thesis is within the 50-page limit and satisfies all font and margin requirements and the thesis contains the following original works:

- Original literature review in Chapter 1 which describes existing techniques used in this work.
- Demonstrated bipartite entanglement of 414 qubits, genuine multipartite entanglement of 14 qubits, and entanglement characterisation of a 127-qubit graph state via new energy estimation algorithm in Chapter 2.
- Doubling the coherence time of graph state using dynamical decoupling in Chapter 3
- Sustained entanglement on a graph state after 11 hops of teleportation in Chapter 4.

Contributions from other works are cited below:

- Results outlined in Section 2.2 are produced using Python codes 50% written up by John. F. Kam and Gary Mooney.
- The interpretation of equation 2.12 is originated from the work of F. Creevey et al.
- 25% of the Python codes for identifying Pauli-strings in powers of Hamiltonian and grouping of TPB sets in Section 2.4.3 is originally from Michael Jones.

# Acknowledgements

I would like to express my greatest appreciation to Prof. Lloyd Hollenberg and Dr. Gary Mooney for their professional and patient supervision throughout my research experience. I am grateful to Lloyd for his invaluable suggestions on my research direction and explanations of questions. I thank Gary for his assistance in technical details, the research progress would not have been as fast without his help. It is also a great pleasure to thank A/Prof. Charles Hill, who provided insightful teaching in the early stage of my research. I would also like to acknowledge John Fidel Kam and Michael Jones for generously sharing their codes. Lastly, I thank Floyd Creevey, for providing interpretations of the formula used in this work.

# Contents

<b>0 Overview</b>	<b>1</b>
<b>1 Introduction</b>	<b>2</b>
1.1 Quantum Computation . . . . .	2
1.2 Quantum Entanglement . . . . .	4
1.3 Physical Quantum Computers . . . . .	5
1.3.1 Technical Routes in Quantum Computers . . . . .	5
1.3.2 Limitations of Noisy Intermediate-Scale Quantum Devices . . . . .	5
1.4 Entanglement Characterisation in NISQ Era . . . . .	6
1.4.1 Graph States . . . . .	6
1.4.2 Quantum State Tomography . . . . .	7
1.4.3 Negativity Estimation of Entanglement . . . . .	9
1.4.4 Fidelity Estimation of Entanglement . . . . .	9
1.4.5 Error Mitigation . . . . .	10
1.4.6 Summary of the Context of This Project . . . . .	12
<b>2 Entanglement Characterisation of Graph States</b>	<b>13</b>
2.1 Introduction . . . . .	13
2.2 Characterisation of Bipartite Entangled States . . . . .	13
2.2.1 A Pathway to Multi-partite Entanglement Using Bipartite Measurements on IBM Quantum Devices . . . . .	13
2.2.2 Verification of QREM reliability . . . . .	17
2.3 Characterisation of Multi-Partite Entangled States . . . . .	20
2.3.1 Fidelity Estimation Using Randomised Stabilisers . . . . .	20
2.3.2 Fidelity Estimation Realisations on IBM Quantum Devices . . . . .	21
2.4 Hamiltonian Moments as an Entanglement Estimation Algorithm . . . . .	23
2.4.1 Energy Estimation using Hamiltonian Moments . . . . .	24
2.4.2 Graph State as an Eigenstate of The Hamiltonian . . . . .	25
2.4.3 Complexity Suppression Using Tensor Product Basis Sets . . . . .	26
2.4.4 Ground State Energies . . . . .	28
2.4.5 Distance to Nearest Eigenstate . . . . .	30
<b>3 Entanglement Preservation of Graph States</b>	<b>31</b>
3.1 Introduction . . . . .	31
3.1.1 Periodic Dynamical Decoupling . . . . .	31
3.2 Extending Graph State Coherence Time . . . . .	33
3.2.1 Improvement of coherence time . . . . .	33
3.2.2 Outlook . . . . .	34
<b>4 Entanglement in Teleportation</b>	<b>35</b>
4.1 Introduction . . . . .	35
4.1.1 One-way Quantum Computation and Teleportation . . . . .	35
4.2 Teleportation of two-qubit Graph State . . . . .	36
4.2.1 Dynamical circuits . . . . .	36
4.2.2 Post-Procession of projected State . . . . .	38
4.2.3 Comparisons with the SWAP Gate Approach . . . . .	40
<b>5 Conclusion and Outlook</b>	<b>43</b>
<b>Bibliography</b>	<b>45</b>

# 0 Overview

This research thesis focuses on the evaluation of quantum algorithms for characterising and verifying entanglement on IBM quantum devices in different approaches. This thesis applies different techniques for benchmarking entanglement, and the results are compared on the advantages and drawbacks of their accuracies and time complexities.

The thesis is comprised of five chapters. The first chapter is an introduction to the background of this research, aiming to give the readers a preliminary understanding of the major concerns of this work and its significance. Some existing background theories including quantum state tomography and error mitigation techniques are also introduced.

The second chapter explores various ways to measure the entanglement of graph states prepared on IBM quantum devices. In this chapter, established from known methodologies such as parallel quantum computation, fidelity estimation using randomised stabilisers, and energy estimation using Hamiltonian moments, major entanglement measurement norms are discussed, and new algorithms are investigated, along with the analysis of their time complexity. The feasibility of using Hamiltonian moments as verification of entanglement is also demonstrated. Particularly, bipartite entanglement of all adjacent qubits on a 414-qubit graph state and a new witness of entanglement across a 127-qubit system is verified.

The third chapter focuses on the preservation of graph states. Utilising the previously discussed norms, techniques that resist the decoherence of quantum states are tested on the graph states while they decay.

In the fourth chapter, based on a known quantum teleportation procedure of dynamical circuits, a new technique of reducing information lost during the teleportation of graph states at different hops is developed. We show that the average decoherence rate of a two-qubit Bell state under such an approach is significantly suppressed when compared against the traditional ‘teleportation’ using SWAP gates.

# 1 Introduction

## 1.1 Quantum Computation

Due to the inherent nature of superposition, entanglement, and measurement-collapse of quantum states, quantum systems involving complex correlations between subsystems are generally found difficult to simulate on classical devices. Therefore, if computers themselves can operate on the basis of quantum mechanics [1], the compute resources of simulating a quantum system are significantly reduced. In fact, there are already quantum algorithms discovered that are proven to be subversive to classical ways, including Shor's factoring algorithm [2], Grover's search algorithm [3], Variational Quantum Eigensolver [4], Quantum Approximate Optimisation Algorithm [5] and Quantum Machine Learning [6]. As a cross-discipline field, unsurprisingly there are many other applications of quantum computation. Several examples may include the simulation of complex molecules and proteins in quantum chemistry [7], quantum machine learning [6, 8], bioinformatics [9], and optimisations in finances [10]. In this section, the basic concepts and their mathematical formalisms of quantum computation will be discussed in detail.

A qubit—the fundamental unit of quantum computation—is commonly described within the mathematical formalism of  $SU(2)$  Lie group, where its matrix representations define the 2-dimensional Hilbert Space it operates on. Specifically, a  $SU(2)$  quantum state has three generators denoted by Pauli operators,

$$X = \begin{pmatrix} 0 & 1 \\ 1 & 0 \end{pmatrix}, Y = \begin{pmatrix} 0 & -i \\ i & 0 \end{pmatrix}, Z = \begin{pmatrix} 1 & 0 \\ 0 & -1 \end{pmatrix} \quad (1.1)$$

such that its group elements are expressed via

$$\exp(i\theta\hat{\mathbf{n}} \cdot \vec{\sigma}) \quad (1.2)$$

where  $\vec{\sigma} = (X, Y, Z)$ ,  $\hat{\mathbf{n}}$  is the unit vector and  $\theta \in (-\pi, \pi]$ . Those operators can be performed as logic gates that act on a quantum state in a row vector,

$$|\psi\rangle = \begin{pmatrix} \alpha \\ \beta \end{pmatrix} = \alpha|0\rangle + \beta|1\rangle \in \mathbb{C}^2, \quad (1.3)$$

where  $|0\rangle$  and  $|1\rangle$  are the eigenstates of the Pauli-Z operator (the common choice of computational basis in quantum computing) and are analogous to binary states in classical computing.

In the language of quantum circuits, blocks connected by horizontal lines represent unitary quantum gates acting on qubits with time evolution from left to right. For example, an operation  $U$  acting on a qubit is expressed as

$$\text{——} \boxed{U} \text{——} \quad (1.5)$$

To express multi-qubit states, it is natural to use tensor products to form a multi-qubit Hilbert space  $\mathbb{H}_1 \otimes \mathbb{H}_2$ ,

$$|a\rangle \otimes |b\rangle = \begin{pmatrix} \alpha_1 \\ \beta_1 \end{pmatrix} \otimes \begin{pmatrix} \alpha_2 \\ \beta_2 \end{pmatrix} = \begin{pmatrix} \alpha_1\alpha_2 \\ \alpha_1\beta_2 \\ \beta_1\alpha_2 \\ \beta_1\beta_2 \end{pmatrix} \equiv \begin{array}{c} |a\rangle \\ |b\rangle \end{array} \quad (1.6)$$

Similarly for multi-qubit gates, to represent independent gates acting on 2 or more qubits, we can express them as tensor products,

$$U_1 U_2 = U_1 \otimes U_2 = \begin{pmatrix} a_1 & b_1 \\ c_1 & d_1 \end{pmatrix} \otimes \begin{pmatrix} a_2 & b_2 \\ c_2 & d_2 \end{pmatrix} = \begin{pmatrix} a_1a_2 & a_1b_2 & b_1a_2 & b_1b_2 \\ a_1c_2 & a_1d_2 & b_1c_2 & b_1d_2 \\ c_1a_2 & c_1b_2 & d_1a_2 & d_1b_2 \\ c_1c_2 & c_1d_2 & d_1c_2 & d_1d_2 \end{pmatrix} \quad (1.7)$$

$$\equiv \begin{array}{c} \text{---} \boxed{U_1} \text{---} \\ \text{---} \boxed{U_2} \text{---} \end{array}.$$

Correlated 2-qubit gates are categorised as those that cannot be represented by any tensor products of  $2 \times 2$  matrices and thus generate entanglement, such as Controlled-NOT (CNOT) gate,

$$\text{CNOT} = \begin{pmatrix} 1 & 0 & 0 & 0 \\ 0 & 1 & 0 & 0 \\ 0 & 0 & 0 & 1 \\ 0 & 0 & 1 & 0 \end{pmatrix} \equiv \begin{array}{c} \text{---} \bullet \text{---} \\ \text{---} \oplus \text{---} \end{array}. \quad (1.8)$$

Additionally, unlike classical computers, the measurement of a quantum system is special. In quantum mechanics, a measurement of a quantum state would in principle perturb it, also known as the collapse of the wavefunction. For example, after measuring a state  $|\psi\rangle = \alpha|0\rangle + \beta|1\rangle$  in the  $Z$ -basis, if the result happens to be  $+1$ , then the state  $|\psi'\rangle$  after the measurement collapse to  $|0\rangle$ , and similarly for a measurement outcome of  $-1$ , the state collapse to  $|1\rangle$ . Mathematically, this measurement is equivalent to a projection to an eigenstate in the direction of measurement,

$$M_m |\psi\rangle = \frac{|m\rangle \langle m|\psi\rangle}{\sqrt{\langle\psi|m\rangle \langle m|\psi\rangle}}. \quad (1.9)$$

According to the probability interpretation, the probability of measuring  $+1$  or  $|0\rangle$  and the probability of measuring  $-1$  or  $|1\rangle$  are  $\|\alpha\|^2$  and  $\|\beta\|^2$ , where  $\alpha$  and  $\beta$  are the coefficients of basis  $|0\rangle$  and  $|1\rangle$  respectively. In a quantum circuit, the measurement operation terminates a circuit wire and appears in a circuit diagram as

$$\text{---} \boxed{\text{A}} \text{---} \quad (1.10)$$

These fundamental units and operations different from classical counterparts together define two major properties of quantum computation and information: superposition and entanglement. By utilising superposition, the theory of quantum computation allows an exponential

increase in the number of states in superposition with a linear increase in the number of qubits. Similarly, conditional transformations like evaluating a function on all possible initial inputs in superposition can be executed in parallel [11], accomplishing quantum parallelism. Yet, there are limitations on the accuracy of the data processed due to noise and problems in extracting full information of a state by reading out at the end of the computation due to the measurement-collapse mechanism mentioned before. As a fundamental property of quantum computing, understanding entanglement in near-term quantum physical devices is a major focus of this work.

## 1.2 Quantum Entanglement

To demonstrate the superiority of classical computers, quantum entanglement is often seen as a key metric that classical computers unable to simulate in a reasonable runtime. Therefore, being able to generate, preserve, and characterise entanglement in a time-efficient way such that entanglement can be verified easily, is key to helping benchmark the capability of fault-tolerance in a quantum device.

Among all the debates about the completeness of quantum mechanics, the famous EPR paradox led by Einstein, Podolsky, and Rosen [12] questions the theory of entanglement. To address this problem, Bell proposed his Bell inequality that is quantitatively measurable to define whether quantum states are entangled by violating the upper bound of any classical systems [13, 14]. Nowadays, the concept of entanglement is well-defined and there are wide applications including dense coding, quantum key distribution, and as the engine of quantum information processing.

Rigorously, a state is biseparable if there exists a bipartition between subsystems  $a_i$  and  $b_i$  of every underlying pure state, where the density matrix can be decomposed by tensor product,

$$\rho = \sum_i^N p_i \rho_i^{a_i} \otimes \rho_i^{b_i}, \quad (1.11)$$

where  $\rho_i^{a_i} = |\psi_i\rangle\langle\psi_i|^{a_i}$  and  $\rho_i^{b_i} = |\phi_i\rangle\langle\phi_i|^{b_i}$  are density matrices of pure states  $i$  of subsystems  $a_i$  and  $b_i$  respectively [15]. For the case where  $a_i = A$  and  $b_i = B$ , the state is said to be separable. A state is *genuinely multipartite entangled*(GME) when it is *non-biseparable*. Similarly, a state has *bipartite entanglement* on a specified bipartition means that its density matrix cannot be decomposed with respect to that bipartition.

Von Neumann entanglement entropy [16] is a standard quantity that can measure the amount of entanglement between two arbitrary partitions  $A, B \in \mathbb{H}$  of a quantum system,

$$S(\rho^A) = -\text{tr}(\rho^A \log_2 \rho^A), \quad (1.12)$$

where  $\rho^A = \text{Tr}_B(\rho)$  is the partial trace of the density matrix  $\rho$  with respect to the partition  $A$ . In other words, this quantity measures how much information is lost or how much entropy will be gained in the partition  $B$  if the partition  $A$  of the state is measured. In the case when  $S = \log_2(d)$ , where  $d$  is the dimension of a quantum system, it corresponds to a maximally mixed state after measurement on partition  $A$  or  $B$ .

## 1.3 Physical Quantum Computers

### 1.3.1 Technical Routes in Quantum Computers

In order to fully unleash the potential of the computational power described in theory, quantum computing architectures have been developed based on varying technologies. For example, quantum computers based on ion traps [17] couple ions to electromagnetic fields. Quantum optics [18] encode photons as qubits. Also, Nitrogen-Vancancy centres that rely on a defect in diamond crystals can encode qubits [19]. Quantum devices built from semiconductors [20] utilise electron or nuclear spins as degrees of freedom. Finally, superconducting qubits [21] use the quantum oscillator energy eigenstates to encode information. Each of those designs has its weak points. For example, semiconductor donors intrinsically exhibit long lifetimes and get backing from the existing semiconductor industry at scale, but the coupling scale is extremely small. In quantum optics, it is generally hard to interact photons together, but it is usually straightforward to manipulate single photon states. Ion traps demonstrate high state fidelity but experience problems such as heating and slow gates. Superconducting qubits face the challenge of relatively fast decoherence time compared to semiconductor donors, in a trade-off with great potential in programmability and scalability.

The experiments that are about to be introduced in this thesis are performed on the IBM Quantum device based on superconducting qubits.

### 1.3.2 Limitations of Noisy Intermediate-Scale Quantum Devices

As the breakthrough of manipulable quantum systems represented by works from IBM [22], Google [23], and USTC [24] reaches a level of a few hundred qubits recently, the preparation of real, large entangled states has become available. Despite that, most quantum algorithms require a substantial number of qubits and high circuit depth to obtain meaningful results and demonstrate quantum advantage against classical computers. For example, to prime factor a 2048-bit integer that approximately has the size of  $O(10^{616})$ , it requires  $O(10^7)$  qubits to implement Shor's algorithm [25]. These demands in universal quantum computation inevitably clash with the fact that state-of-the-art quantum computers are in a noisy intermediate scale quantum (NISQ) era, which essentially means that although we have access to quantum devices with several qubits up to intermediate-scale, the high quantum gate error rate severely affects the implementation of potential applications. For example, quantum volume (QV) as a benchmark for measuring the error rate of NISQ quantum devices, is only achieved up to  $2^{19}$  [26], meaning that a quantum circuit can be executed at a maximum with only 19 qubits and total depths of 19 on random two-qubit gates simultaneously while producing a reasonable fidelity of the result greater than 2/3.

As a result, the development of quantum error correction becomes crucial in stepping towards universal quantum computation from the regime of NISQ devices. Quantum error correction works have been done by encoding many physical qubits into a logical qubit and producing robustness against errors by correcting them using ancilla qubits in which the syndromes are

measured. Such types of strategies are also known as the quantum error-correction surface codes [27–30]. However, since this approach trades off the number of qubits required for the robustness of the logical qubit, at the current typical gate error rate at the level of 1%, it requires thousands of physical qubits to encode a single logical qubit. However, studies that approximate the resources required for fault-tolerant quantum computing on surface code assume that a physical error rate below 0.1% is plausibly achievable for quantum hardware while enabling error correction [25].

## 1.4 Entanglement Characterisation in NISQ Era

It is challenging to make qubits filtered from environmental disturbance while forcing strong couplings among them in the Noisy Intermediate-Scale Quantum (NISQ) era. Therefore, the ‘quality’ rather than the ‘quantity’ of qubits and gates prepared is what we should care more about [31]. Focusing on producing larger entangled states and improving the strategies for measuring entanglement is one way to measure the progress and capabilities of quantum computers while accomplishing quantum advantage. Efforts have been made recently to demonstrate the generation of large-entangled states, including the demonstration of nearest-neighbour bipartite entanglement [15, 32, 33], genuine multipartite entanglement on stabiliser states up to a size of 51 qubits [24], and 18-qubit Greenberger-Horne-Zeilinger (GHZ) state [34] on superconducting quantum devices, as well as 32-qubit GHZ states [35] prepared on ion-trap quantum devices built by Quantinuum. Precisely and efficiently characterising the entanglement of various states using different metrics can act as tools for physicists to test whether a quantum computer matches its designs, hence quickly identifying any problems and providing hints for the next-step improvements. Unlike typical benchmarking metrics such as  $T_1$ ,  $T_2$ , CLOPS [36], and quantum volume [37] that only address the performance of a quantum computer in general, benchmarking the entanglement of some specific quantum states allows researchers to understand the performance of a quantum computer under particular conditions, which helps to characterise typical gate or readout noises located at designated qubit [38]. Next, to address this topic, we introduce some fundamental concepts and formalisms that are relevant to entanglement characterisation.

### 1.4.1 Graph States

Graph states are a group of quantum states that can be mapped onto a graph, where each vertex represents a qubit and each edge forms a coupling between the incident qubits [39]. Graph states have been shown to be more robust against local measurement and noise [40]. Formally, a graph state mapped from a graph  $G = (V, E)$  is defined as

$$|\phi(G)\rangle = \prod_{(\alpha,\beta) \in E} CZ_{(\alpha,\beta)} |+\rangle^{\otimes n}, \quad (1.1)$$

where  $|+\rangle = \frac{1}{\sqrt{2}}(|0\rangle + |1\rangle)$  is the positive Pauli- $X$  eigenstate,  $n = |V|$  is the number of qubits and  $CZ_{(\alpha,\beta)}$  is the controlled- $Z$  gate acting on edge  $(\alpha, \beta)$  of the graph  $G$ . At the same time,

there is a set of stabiliser generators that can also uniquely define a graph state,

$$\{K_\alpha := X_\alpha \prod_{\beta \in N(\alpha)} Z_\beta | \alpha \in V(G)\}, \quad (1.2)$$

such that only the graph states can be stabilized by them,

$$K_\alpha |\phi(G)\rangle = |\phi(G)\rangle. \quad (1.3)$$

An essential property of a graph state is that the original graph state can be projected into a separable state comprised of a Bell state on two neighbouring qubits and another collapsed state on the rest of the qubits simply by measuring all but except the two neighbouring qubits in the Pauli-Z basis.

$$|\phi(G)\rangle \mapsto |\text{Bell}\rangle_{(\alpha,\beta)} \otimes |s_1 s_2 \cdots s_{\alpha-1} s_{\alpha+1} \cdots s_{\beta-1} s_{\beta+1} \cdots s_{n-1} s_n\rangle, \quad (1.4)$$

where  $(\alpha, \beta) \in E$  is an arbitrary pair of neighbouring qubits incident to an edge of the graph and  $s_i$  is the state on the  $i^{\text{th}}$  projected qubit. This allows us to measure the entanglement of each pair of neighbouring qubits which has been done in [32, 33] using the negativity (see detail in Section 1.4.3).

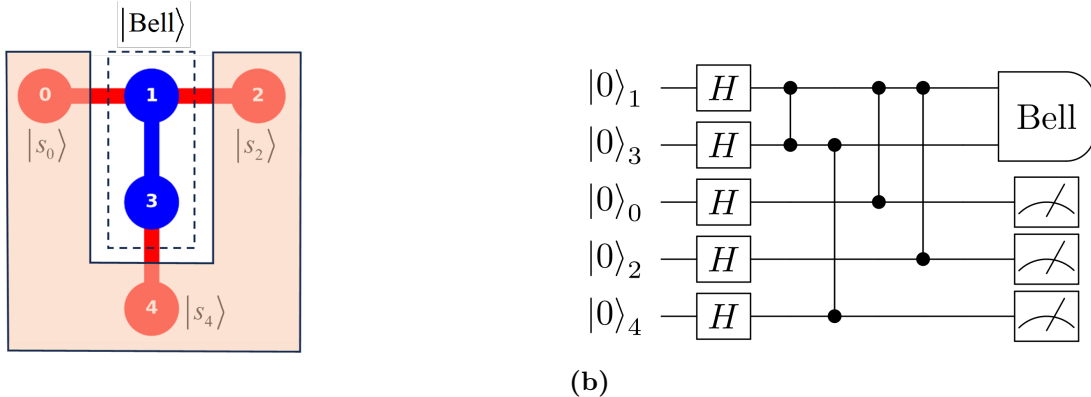


**Figure 1.1:** (a) The coupling map/native graph  $G$  of `ibmq_quito` comprises a total of five labelled qubits/vertices with edges  $E(G) = \{(0,1), (1,2), (1,3), (3,4)\}$ . Qubit 0, 2, and 4 are measured in  $Z$ -basis with outcome  $|s_0\rangle \otimes |s_2\rangle \otimes |s_4\rangle$ , and qubit 1, 3 are left with a Bell state up to local transformations (b) Corresponding circuit diagram of the native graph state and Bell state projection

Other properties include naturally adaptive to quantum teleportation, which can teleport states along paths in the graph by projecting intermediate qubits [41], quantum error correction codes, and CSS codes in secret-sharing [42], which all make graph states play a crucial role in quantum computation.

### 1.4.2 Quantum State Tomography

In order to obtain reasonable estimates of the entanglement qualities of graph states, we employ multiple algorithms that use different parameters, including negativity and fidelity (see detail

in Section 1.4.4). In those algorithms, obtaining the estimated density matrix of the desired state is a crucial step. Quantum state tomography (QST) is one of the most important methods to reconstruct the density matrix for relatively small systems.

In QST, the expected values of all possible Pauli-operator combinations are used to reconstruct the density matrix of a state [16],

$$\rho = \sum_{\vec{v}} \frac{\text{Tr}(\sigma_{v_1} \otimes \sigma_{v_2} \otimes \cdots \otimes \sigma_{v_n} \rho) \sigma_{v_1} \otimes \sigma_{v_2} \otimes \cdots \otimes \sigma_{v_n}}{2^n} = \sum_{\vec{v}} \frac{\text{Tr}(\sigma_{\vec{v}} \rho) \sigma_{\vec{v}}}{2^n}, \quad (1.5)$$

where  $\vec{v} = (v_1, v_2, \dots, v_n)$ , and  $v_i \in \{0, 1, 2, 3\}$  is the label of the three Pauli operator or identity acting on the  $i^{th}$  qubit,  $n$  is the number of qubits involved. To compute the expected value of any given Pauli observable combination string concerning a prepared quantum state, each qubit of the quantum state is measured in that Pauli basis corresponding to its position in the string, and the probabilities of outcomes are sampled. In practice, instead of physically measuring any qubit in different directions, the measurement of a qubit in basis  $O$  other than  $Z$  is achieved by changing the basis acting on the state itself. After the change of basis, any information of the state on the qubit originally expressed in  $|\pm\rangle$  or  $|\pm i\rangle$  will now be in  $|0\rangle$  and  $|1\rangle$ . Hence, measurement can be performed as usual in  $Z$ -basis, but the data obtained is about the original basis  $O$ . Therefore, the expected value with respect to a specific Pauli observable  $\vec{v}$  is expanded as

$$\text{Tr}(\sigma_{\vec{v}} \rho) = \sum_{s_1, s_2, \dots, s_n} (-1)^{s_1 + s_2 + \cdots + s_n} P_{\vec{v}}^{(s_1, s_2, \dots, s_n)} \quad (1.6)$$

and

$$1 = \sum_{s_1, s_2, \dots, s_n} P_{\vec{v}}^{(s_1, s_2, \dots, s_n)}, \quad (1.7)$$

where  $P_{\vec{v}}^{(s_1, s_2, \dots, s_n)}$  is the probability of obtaining a measurement outcome of  $|s_1, s_2, \dots, s_n\rangle$  with respect to the Pauli observable  $\vec{v}$ , and  $s_i \in \{0, 1\}$  is the measurement outcome of the  $i^{th}$  qubit. In practice, the probability is approximated by the number of outcomes that has the readout  $|s_1, s_2, \dots, s_n\rangle$  divided by the total shots, and all possible outcomes should sum to unity. Notably, each measurement outcome contributes positively if there are even numbers of  $|1\rangle$  or contributes negatively if there are odd numbers of  $|1\rangle$ . This is due to the fact that for each eigenstate  $|1\rangle$  in its given basis, the eigenvalue is  $-1$ .

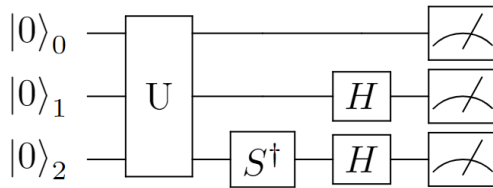


**Figure 1.2:** Example circuit that measures qubits 0, 1, and 2 in the  $Z, X$  and  $Y$  bases respectively

However, the computing complexity of full QST is exponential with the qubit count, namely  $O(3^N)$ . To bypass the exponential requirement on resources, a way is to find entanglement witnesses that can detect entanglement from only a few observables but are engineered only to respect specific target states. Unlike QST, the number of measurements in an entanglement

witness does not grow exponentially with the number of qubits in the state. This approach was already implemented in [15, 43]. Also, a more efficient algorithm is adapted from QST using randomly generated operators from stabilisers [44], which is also studied in this thesis.

### 1.4.3 Negativity Estimation of Entanglement

To quantify the amount of entanglement between bipartitions  $a_i$  and  $b_i$  in any mixed state, where  $i$  is the label of the  $i^{th}$  underlying pure state (see Section 1.2), one can employ an entanglement measure by calculating the negativity [45] of the state with respect to some bipartitions. For a given density matrix  $\rho$  of a quantum system, its negativity  $\mathcal{N}(\rho)$  with respect to a fixed bipartitions  $a$  and  $b$  is given by

$$\mathcal{N}(\rho) = \frac{1}{2}(\|\rho^{T_a}\| - 1) = \left| \sum_{\lambda_i < 0} \lambda_i \right|, \quad (1.8)$$

where  $\lambda_i$  are the negative eigenvalues of partial transpose  $\rho^{T_a}$  of subsystem  $a$ . Note that the bipartitions are set artificially, which does not imply the respective quantum state's separability. The partial transpose [46] of a matrix is the transpose of the sub-matrix acting only on the sub-Hilbert space as if it can be decomposed like a separable state. In terms of its definition, if a matrix  $\rho$  acting on the Hilbert space  $\mathbb{H}_1 \otimes \mathbb{H}_2$  has the form

$$\rho = \sum_{ijkl} M_{ijkl} |i, j\rangle \langle k, l| = \sum_{ijkl} M_{ijkl} |i\rangle \langle k| \otimes |j\rangle \langle l|, \quad (1.9)$$

where  $|i\rangle \langle k|$  is defined on  $\mathbb{H}_1$  and  $|k\rangle \langle l|$  is defined on  $\mathbb{H}_2$ , its partial transpose is simply a transpose on one of the sub-Hilbert space. For example,

$$\rho^{T_{\mathbb{H}_1}} = \sum_{ijkl} M_{ijkl} |k\rangle \langle i| \otimes |j\rangle \langle l|, \quad (1.10)$$

and similarly,

$$\rho^{T_{\mathbb{H}_2}} = \sum_{ijkl} M_{ijkl} |i\rangle \langle k| \otimes |l\rangle \langle j|. \quad (1.11)$$

Negativity sums over all negative eigenvalues of the partial transpose of  $\rho$ . It is equal to 0 if the state is separable since  $\|\rho^{T_{\mathbb{H}_1}}\|$  or  $\|\rho^{T_{\mathbb{H}_2}}\| = 1$  for all separable systems, and it is equal to 0.5 for a maximally entangled state. Therefore for any given mixed state with bipartition, it is entangled if one can measure their negativity to be greater than 0.

### 1.4.4 Fidelity Estimation of Entanglement

Different from measuring the negativities of bipartite systems projected from a larger entangled state, calculating its fidelity would be a more direct approach in practice [47]. Unlike the negativity that only check the amount of entanglement between specific partitions, fidelity measures how well a noisy quantum state is generated with respect to its ideal state as a whole

and can be used as an entanglement witness to detect GME. Specifically, the fidelity  $F$  of any prepared (noisy) state  $\rho$  with respect to its ideal target state  $\rho^{ideal}$  is defined as

$$F(\rho, \rho^{ideal}) = \text{tr}(\rho\rho^{ideal}) = |\langle \Psi | \Psi^{ideal} \rangle|^2, \quad (1.12)$$

where  $\rho$  and  $\rho^{ideal}$  are density matrices of state  $|\Psi\rangle$  and  $|\Psi^{ideal}\rangle$  respectively. As suggested in its form, this measures the overlap between the prepared and target states. From this, one can quantify how close the noisy state is to the ideal case. Most importantly, the fidelity of more than 0.5 is a **sufficient** condition for demonstrating GME for the given state.

### 1.4.5 Error Mitigation

In the NISQ era, a major source of error for IBM Quantum superconducting devices is the readout assignment error, which essentially is reading a measurement outcome falsely to be  $|0\rangle$  or  $|1\rangle$  when it should be  $|1\rangle$  or  $|0\rangle$ . For large quantum states, the accumulated readout error of the entire state can be overwhelming, even if the readout error per qubit is small. To compensate for this, an error mitigation technique called Quantum Readout Error Mitigation (QREM) [48] is applied throughout this work. For simplicity of analysis, we ignored other sources of errors such as correlated errors/cross talks and gate errors, which contribute minorly and are often a good approximation to assume errors are caused by faulty measurement, not faulty state preparation [47]. Therefore, the errors are independently calibrated by assuming that the readout assignment errors are perfectly independent of each qubit. In the model of QREM, a set of measured outcomes with respect to a particular quantum circuit is expressed in a row vector such that each element in the vector represents the probability of some specific outcome,

$$\vec{p}_{\text{noisy}} = \sum_{s_1, s_2, \dots, s_n} p_{s_1, s_2, \dots, s_n} \bigotimes_{i=1}^n \begin{pmatrix} 1 - s_i \\ s_i \end{pmatrix} \quad (1.13)$$

where the sum is over all state combinations  $s_1, s_2, \dots, s_n$  and the position of an outcome in the vector is represented by its corresponding  $n$ -qubit quantum state in vector form. An example of measuring an outcome of  $|01\rangle$  in two-qubit system would be a vector  $\begin{pmatrix} 1 \\ 0 \end{pmatrix} \otimes \begin{pmatrix} 0 \\ 1 \end{pmatrix}$ .

A simulated calibration matrix that maps the ideal probability vector to the noisy probability is defined as

$$\vec{p}_{\text{noisy}} = \boldsymbol{\Lambda} \vec{p}_{\text{ideal}} \quad (1.14)$$

where  $\vec{p}_{\text{ideal}}$  is the ideal probability vector as if all measurements are done correctly without readout errors and  $\boldsymbol{\Lambda}$  is the calibration matrix of dimension  $2^n \times 2^n$ , in which the matrix element of row  $i$  and column  $j$  is interpreted as the probability of measuring  $j$  as  $i$  after translating the outcome bitstring from binary to decimal. It is to be aware that although the calibrated probability is labelled as ‘ideal’, this does not mean this circuit has no error. One should still note this only corrects readout assignment errors. By simply inverting the matrix, the presumed ideal probability vector can be reverse-engineered as

$$\vec{p}_{\text{ideal}} = \boldsymbol{\Lambda}^{-1} \vec{p}_{\text{noisy}}. \quad (1.15)$$

Since we assume there is no correlation between readout errors, the full calibration matrix  $\Lambda$  can be decomposed as tensor products of simple  $2 \times 2$  calibration matrices for each qubit,

$$\Lambda = \bigotimes_{i=1}^n \Lambda_i, \quad (1.16)$$

where  $\Lambda_i$  is the calibration matrix of the  $i^{th}$  qubit in the system, such that  $\vec{p}_{i,\text{ideal}} = \Lambda_i^{-1} \vec{p}_{i,\text{noisy}}$  maps the noisy probability vector to ideal probability vector specifically for qubit  $i$ . By decomposing and decoupling the full calibration matrix, the number of measurements needed to construct it is significantly reduced from exponential  $O(2^n)$  to linear  $O(2n)$ . Also, by assuming there are no correlated errors, calibration data of every qubit can be measured simultaneously. That is, only two circuits that initialize the states in  $|0\rangle^{\otimes n}$  and  $|1\rangle^{\otimes n}$  need to be measured.

Nevertheless, the dimension of the full calibration matrix still grows exponentially with respect to the size of the state, namely  $2^n \times 2^n$ . To avoid the problem of growing spatial complexity, we also implement the “stochastic calibration” technique where necessary, which is first introduced in [47]. Instead of calibrating all qubits simultaneously, this method corrects the probability vector qubit-wisely. Within each iteration, only the components relevant to qubit  $i$  are corrected,

$$\begin{pmatrix} p'_{(s_1, \dots, s_{i-1}, 0, s_{i+1}, \dots, s_n)} \\ p'_{(s_1, \dots, s_{i-1}, 1, s_{i+1}, \dots, s_n)} \end{pmatrix} = \Lambda_i^{-1} \begin{pmatrix} p_{(s_1, \dots, s_{i-1}, 0, s_{i+1}, \dots, s_n)} \\ p_{(s_1, \dots, s_{i-1}, 1, s_{i+1}, \dots, s_n)} \end{pmatrix} \quad (1.17)$$

where all the probabilities corresponding to bit strings  $s_1, \dots, s_{i-1}, 0, s_{i+1}, \dots, s_n$  and  $s_1, \dots, s_{i-1}, 1, s_{i+1}, \dots, s_n$  are mapped to the mitigated probabilities  $p'$ . Therefore, the dimension of a stochastic calibration matrix is only  $2 \times 2$ . However, the number of non-zero probabilities almost doubles in each iteration, especially for sparse vectors. Because of that, a threshold limit  $\epsilon$  is set to artificially zero out each probability below it. After setting the threshold limit, the memory needed to mitigate  $\vec{p}_{\text{noisy}}$  is bounded by  $O(\epsilon^{-1})$  from above.

**Algorithm 1** An algorithm that calculates the closest physical density matrix

**Input:** Unphysical (in principle)  $d \times d$  density matrix  $\rho$  with ordered eigenvalues  $\mu_i$  and corresponding eigenvectors  $|\mu_i\rangle$ ,  $i \in \{1, 2, \dots, d\}$

**Output:** Closest physical density matrix  $\rho' = \sum_i \lambda_i |\lambda_i\rangle \langle \lambda_i|$  with all eigenvalues  $\lambda_i \geq 0$

- 1: Let  $i = d, a = 0$
- 2: **for**  $i = d, d - 1, \dots, 1$  **do**:
- 3:     **if**  $\mu_i + \frac{a}{i} \leq 0$  **then**:
- 4:          $\lambda_i \leftarrow 0$
- 5:          $a \leftarrow a + \mu_i$
- 6:     **else**:
- 7:         **for**  $j \leq i$  **do**:
- 8:              $\lambda_j \leftarrow \mu_j + \frac{a}{i}$
- 9:         **end for**
- 10:     **end if**
- 11: **end for**
- 12: Output  $\rho' = \sum_i \lambda_i |\lambda_i\rangle \langle \lambda_i|$ , where the eigenvectors remain unchanged

---

**Algorithm 2** An algorithm that calculates the closest physical probability vector

---

**Input:** Unphysical (in principle) probability vector  $\vec{P}$  with ordered elements  $x_i$  in an increasing order  $i \in \{1, 2, \dots, L\}$ ,  $\sum_{i=1}^L x_i = 1$

**Output:** Closest physical probability vector  $\vec{P}'$  with all  $x'_i \geq 0$

```

1: Let  $I = \emptyset, n = L$ 
2: for  $i = 1, 2, \dots, L$  do:
3:   if  $x_i + \frac{1 - \sum_{j \in I} x_j}{n} < 0$  then:
4:      $x'_i = 0$ 
5:      $I \leftarrow I \cup \{i\}$ 
6:      $n \leftarrow n - 1$ 
7:   else:
8:      $x'_i = x_i + \frac{1 - \sum_{j \in I} x_j}{n}$ 
9:   end if
10: end for
11: Output  $\vec{P}' = (x'_1, x'_2, \dots, x'_L)^T$ 

```

---

Apart from QREM, other error correction techniques are implemented in this work but do not target quantum errors. An example is [49] described in Algorithm 1, which transforms an unphysical density matrix caused by additive Gaussian noise, including those with negative eigenvalues, to a new matrix without negative eigenvalues. Another similar algorithm is [50] illustrated in Algorithm 2, which approximates unphysical probability vectors, including those elements that become negative after calibration due to sampling fluctuations, to a physical vector.

#### 1.4.6 Summary of the Context of This Project

In summary, as being part of many researches that pave the way toward fault-tolerant quantum computation in the Noisy Intermediate-Scale Quantum (NISQ) era, the main contribution of this thesis is to benchmark the capabilities of near-term quantum devices on their quality of entanglement on large quantum states. Specifically, we verify the generation of bipartite entanglement of neighbouring qubits on graph states and push the record to a system of 414 qubits. We also investigate whole-device entanglement using the method of randomised stabilisers and prove the generation of 14-qubit genuine multipartite entanglement. Additionally, we explore the power of calculating ground state energy from Hamiltonian moments as a way of examining the preparation of quantum states, which has yet to be done before. We study the preservation of the graph state by doubling the characteristic fidelity decoherence time. Utilising measurement-based quantum computation, we develop a new method of teleporting a two-qubit graph state that performs more accurately than traditional swap gates. The next chapter of the thesis will discuss different approaches to characterising multi-partite entanglement in detail.

# 2 Entanglement Characterisation of Graph States

## 2.1 Introduction

Since quantum algorithms with low entanglement can be classically simulated efficiently, high levels of entanglement are generally required to demonstrate quantum advantage. Therefore, we aim to generate and characterise highly entangled quantum states which benchmark a quantum computer. From all candidates, we chose to prepare graph states because of their high entanglement, short circuit depth and resilience in noise. In the case of ideal graph states, the entanglement entropy [16] of all possible bipartitions are maximised. The maximised entropies of the bipartitions in ideal graph states enable us to preserve highly correlated states as much as possible after any noise contaminations. Moreover, the gap measured between actual and ideal bipartite entanglement is an indicator of the level of noise that has affected the process.

In this chapter, we evaluate different entanglement estimation algorithms and develop new adaptations, together with the analysis of their accuracy and complexity. Thanks to the high scalability of the algorithm used in [32, 33] that generated 65 and 127-qubit graph states, we verify the generation of bipartite entanglement on all adjacent pairs of qubits in the record-breaking graph state of 414 qubits created on *ibm\_seattle* [22] using negativity as the parameter. Also, adapting the randomised fidelity estimation algorithm [44] of QST, we demonstrate the genuine multipartite entanglement of graph states up to 14 qubits. Furthermore, inspired by the algorithm developed for variationally estimating energy from moments [51], we explore the possibility of using the ground-state energy of the well-defined Hamiltonian to examine how well the state is prepared from another perspective. The open-source code is available on GitHub [https://github.com/KangHaiYue/MSc\\_Project/tree/main](https://github.com/KangHaiYue/MSc_Project/tree/main).

## 2.2 Characterisation of Bipartite Entangled States

In this section, we employ the method recently introduced in [32] and [15] to characterise bipartite entanglement of all adjacent qubit pairs on the 414-qubit graph state, which is prepared on the IBM Quantum device *ibm\_seattle*. By demonstrating non-zero average negativities on the Bell states, our result certifies the successful generation of bipartite entanglement on all nearest-neighbour qubit pairs in a system of 414 qubits. We also further conduct a series of confidence tests to justify that QREM does not over-correct.

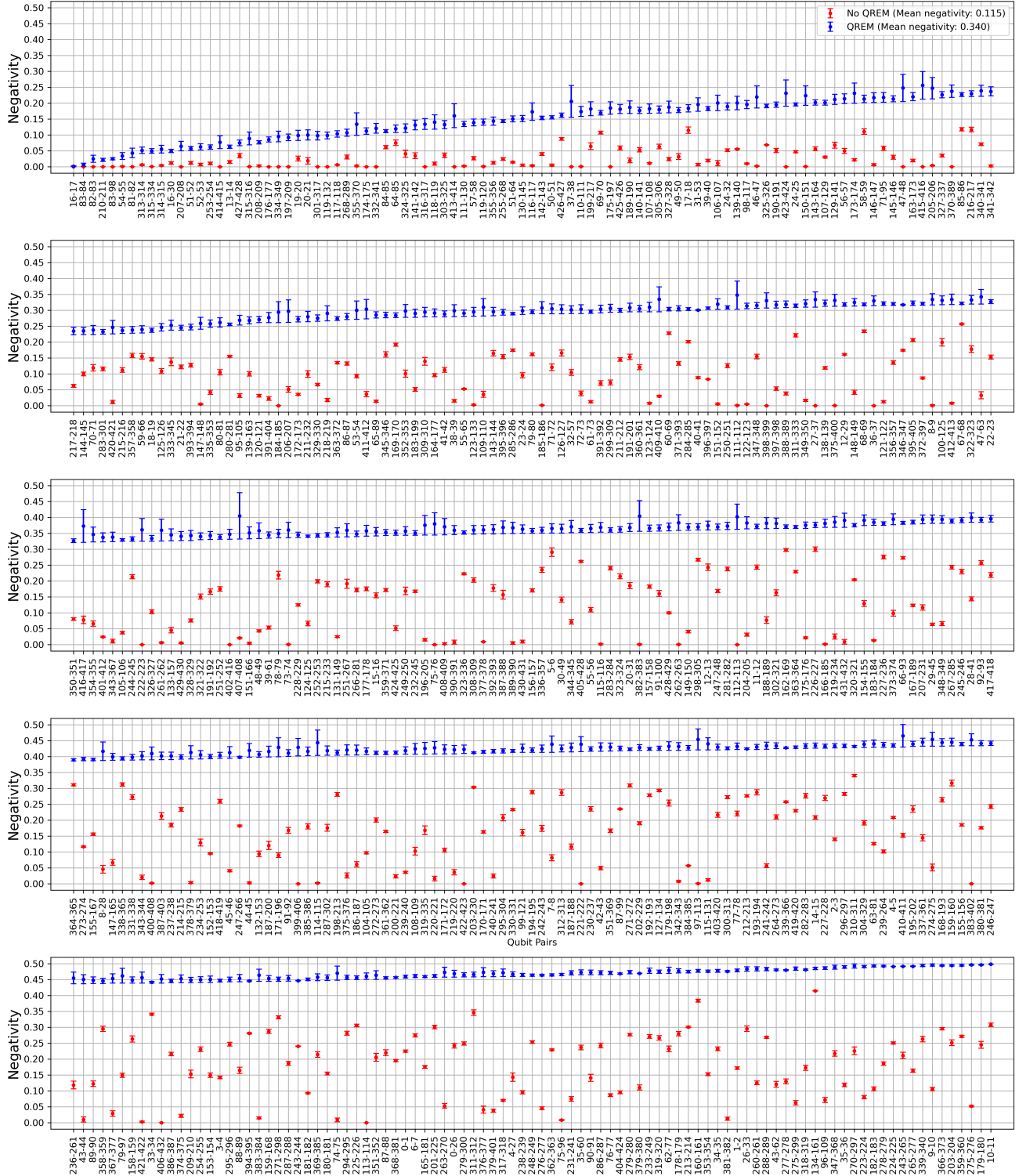
### 2.2.1 A Pathway to Multi-partite Entanglement Using Bipartite Measurements on IBM Quantum Devices

We follow the steps from [32] to characterise bipartite entanglement on all adjacent pairs of qubits but on a much larger graph state of 414 qubits prepared on the IBM Quantum 433-qubit QPU *ibm\_seattle*. In the first step, we generate the corresponding whole-device graph



**Figure 2.1:** The topology for the 414-qubit graph state. Each circle represents a qubit. A qubit is inactive if it is coloured grey. Each colour of the edges represents a group of parallel  $CZ$  gates applied to the qubits incident to them in the same time step. The overall  $CZ$  gate depth is 3.

state from the topology of the device. Since *ibm\_seattle* uses the same physical topology of the heavy-hexagonal lattice as the previous generation 127-qubit *Eagle* processor, the maximum  $CZ$  gate depth to construct any graph state on this device is 3. In actual circuits, instead of using the  $CZ$  gate, *ibm\_seattle* uses the ECR gate as the basis coupling gate designed for minimising drift errors as opposed to traditional  $CNOT$  gates, which can be converted from  $CZ$  gate using local operations [52]. Figure 2.1 illustrates an example of the prepared graph state's topology. Next, we project multiple Bell states simultaneously that do not share the same neighbours by implementing Parallel QST [32] to reconstruct density matrices. In this way, we can simultaneously perform QST on a set of Bell states as mentioned in Section 1.4.2 in the one circuit. Therefore, by grouping each arrangement of projections into batches, the total number of circuits required can be drastically reduced. In our work, there are a total of 8 batches for the 414-qubit graph state, and hence 72 circuits with 2000 shots each to perform one trial of QST on all nearest-neighbour Bell states, compared to a total of 4275 circuits if it is not done in parallel. Here, we complete four trials in total. During this process, we apply QREM and Algorithm 1 previously mentioned in Section 1.4.5. After all, the negativities are calculated using Equation 1.8 described in the Literature Review.



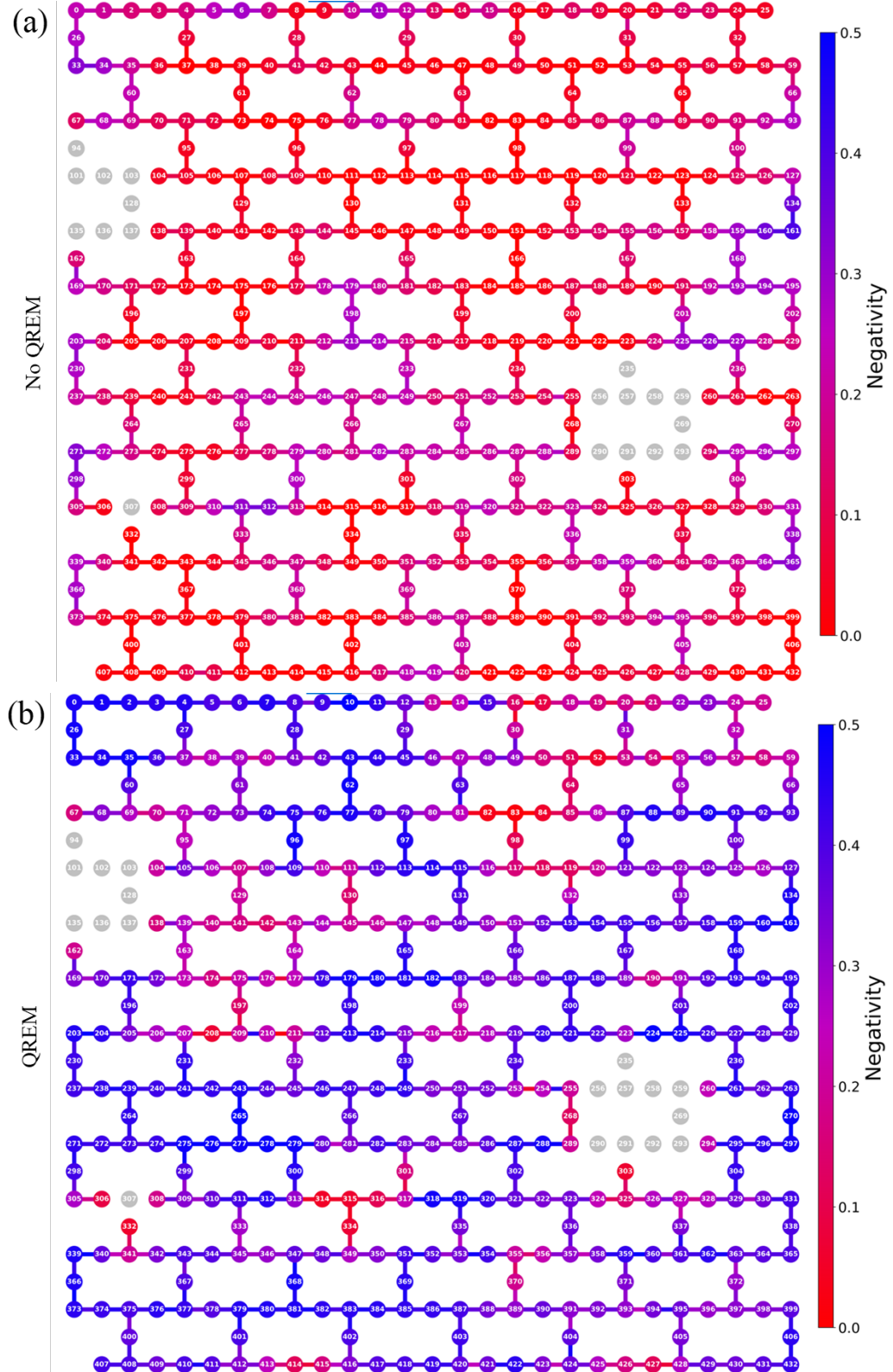


**Figure 2.3:** The corresponding coupling map of the negativities before (a) and after (b) mitigation. Nodes represent the qubits, and edges represent their connections. The colour of an edge indicates the average negativity of the Bell states on the qubits incident to it, and the colour of each qubit is based on the average negativities of nearby edges for a smooth transition between edges.

Although this approach is unable to demonstrate GME as it only considers pairs of neighbouring qubits, whereas the GME criterion requires showing there is a pure state in the mixture that is entangled across all qubits, the number of shots required outperforms the work done in [24]. In that work, a total of  $4.3992 \times 10^8$  shots are completed in 31 hours to fully characterise a stabiliser state of 51 qubits. In contrast, only  $1.44 \times 10^5$  shots completed in less than 4 minutes per trial are required in our work to characterise bipartite entanglement of all nearest-neighbour pairs from 414 qubits. Therefore, the parallel quantum state tomography method is more adaptive under limited resources and can be executed in a much shorter period.

In Figure 2.2, we display the plot of the average negativity versus nearest-neighbour qubit pairs. As shown, the average negativity is given by 0.115, and this improves significantly to 0.340 after QREM, further justifying the assumption from [47] that readout errors play a dominant role in the errors after measurement. Also, we note that the mitigated negativity of bipartitions are all above 0.

A more intuitive approach to present this is via Figure 2.3, which depicts how well qubits are coupled with respect to the heavy-hexagonal architecture of the quantum processor more clearly. In this coupling map, the more blue the edges are, the higher the negativities are measured. As shown in Figure 2.3, most of the qubit pairs have a low level of entanglement before QREM, with 131 edges having negativity below 0.025, where we consider it to be a conservative estimation of measured negativity resolution from trials. However, it is evident that most edges reveal stable entanglement after QREM as in Figure 2.3, despite low negativity edges being clustered together in some regions. Those regions' bad couplings are likely caused by relatively high local CZ gate error rates and noises. It is also noteworthy that several inactive qubits are represented by grey nodes, which limits the size of the producible graph state from 433 qubits to 414 qubits. Despite inactive qubits, all edges have shown their negativities to be above zero as long as any incident qubits are functional.

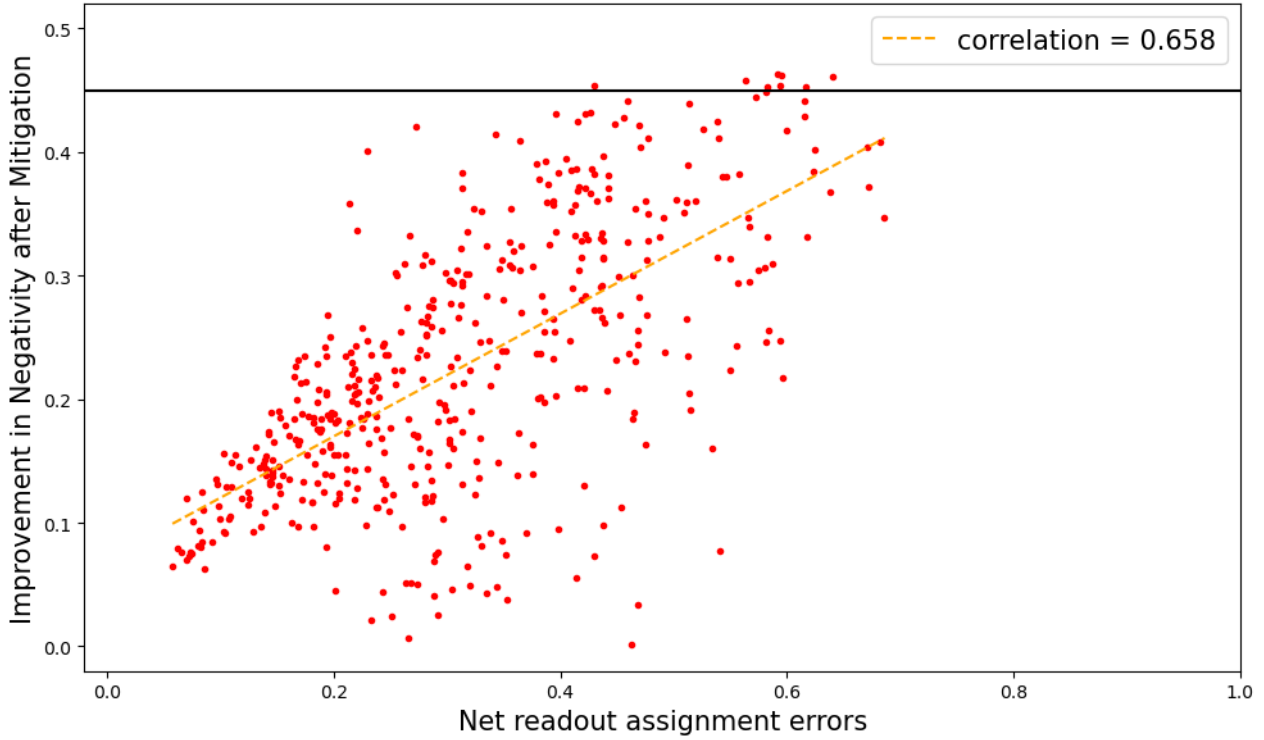
### 2.2.2 Verification of QREM reliability

However, it is natural to question the reliability of QREM in terms of the amount of improvement in the negativity. When some specific pair of qubits exhibit extremely low and high negativity that differs by  $> 0.45$  before and after QREM, it is a concern that whether QREM is over-correcting what it should not be in such a scenario. To address this issue, we first ask if it is true that, on average higher net readout errors of the Bell states and its projected neighbouring qubits lead to a more significant improvement in negativity after QREM.

To answer this question, we first define the term net readout error as one minus the product of the ‘probability of correctness’ for all participating qubits of labels in the set  $V$ ,

$$\epsilon_{\text{net}} = 1 - \prod_{i \in V} (1 - \epsilon_i), \quad (2.1)$$

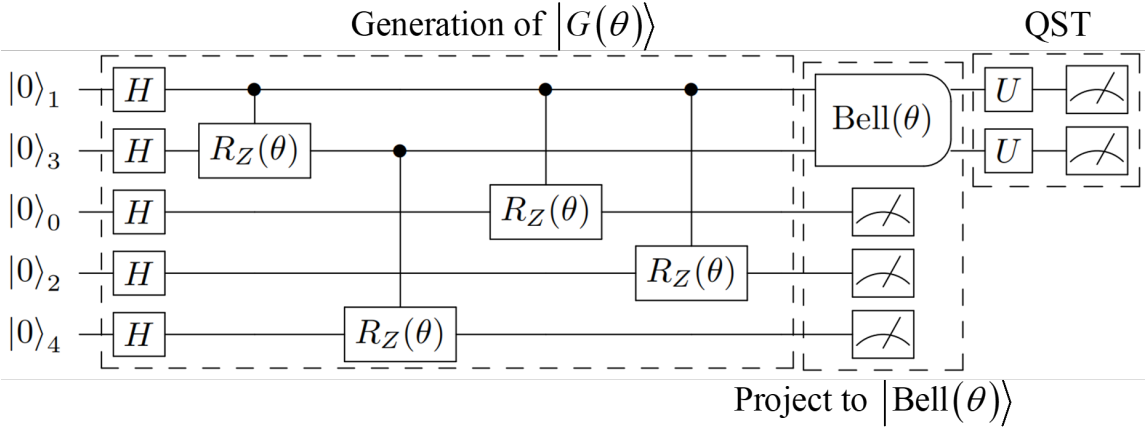
where  $\epsilon_i$  is the measured readout error of qubit of label  $i$ . The data of the readout errors are accessed from IBM Quantum cloud service via <https://quantum-computing.ibm.com/>. Hence, by plotting the negativity against the net readout errors for each Bell state pair in



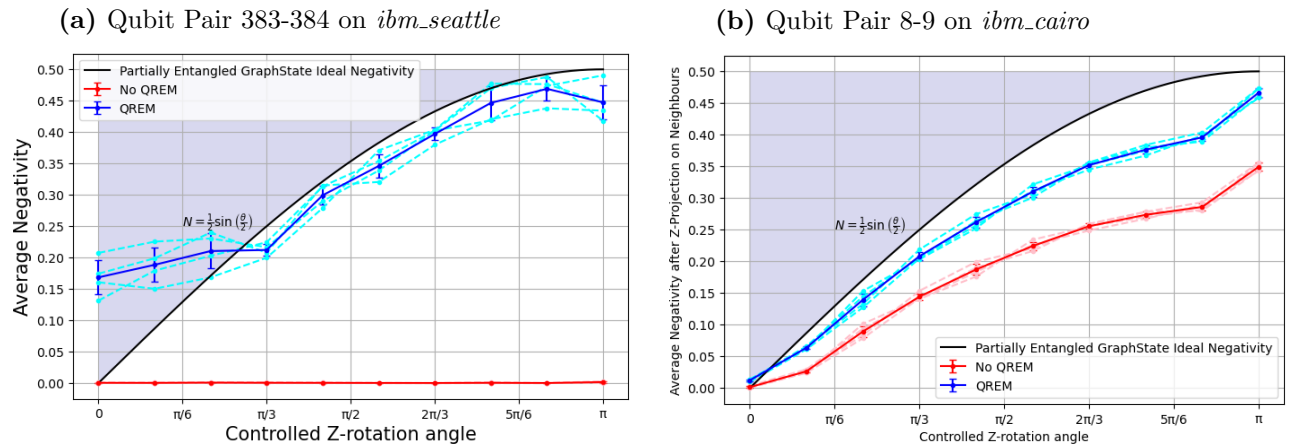
**Figure 2.4:** Plot of the correlation between net improvements in negativity after QREM and net readout errors. Each red dot represents a pair of neighbouring qubits, and the yellow dashed line represents the line of best fit. The correlation coefficient is calculated to be 0.658, indicating a strong, positive correlation. The horizontal black line is a reference for improvements in the negativity of 0.45, which we consider as extreme.

Figure 2.4, we observe a strong correlation of 0.658 between the amount of improvement in negativity  $\mathcal{N}_{\text{QREM}} - \mathcal{N}_{\text{No QREM}}$  to the net readout error. Moreover, the plot also indicates that one would need a net readout error of at least 0.4 to have an improvement in negativity over 0.45, which confirms there are large contributions from readout errors that can be corrected. The net readout error of 0.4 also implies on average, the readout error of each qubit involved in projecting a Bell state is at least 9.71%, a number significantly higher than the median readout error rate of 5.58% at the time of measurement. Therefore, it is strong evidence that big improvements in negativity are indeed correcting those qubits with more readout errors.

Similarly, we want to know if the mitigated negativity close to its theoretical upper bound is over-correcting. However, because 0.5 is both the ideal Bell state negativity and the maximum negativity of any density matrices, we seek other states that are less entangled ideally. Therefore, to further demonstrate the validity of QREM, we conduct tests on partially entangled Bell states projected on the qubit pair (383, 384), which are chosen specifically because of their extremely high improvements in negativity (0.448). Instead of trying to produce maximal entanglement by applying  $CZ$  gate, we deliberately entangle those two qubits by  $CR_Z(\theta)$  as in Figure 2.5. That is controlled-Z rotations by some angle  $\theta$  less than  $\pi$ . This modified ‘Bell state’ is denoted as  $|\text{Bell}(\theta)\rangle$ . Therefore, by artificially constraining the theoretical negativity to below 0.5, this test aims to compare whether the measured negativities exceed the curve of the ideal upper limit,  $\frac{1}{2} \sin\left(\frac{\theta}{2}\right)$ .



**Figure 2.5:** Circuit diagram of the generation of graph state  $|G(\theta)\rangle$  using  $CR_Z(\theta)$  (with global phase of  $\frac{\theta}{2}$ ) instead of  $CZ$  on the same structure as in Figure 1.1. It is then projected into a partially entangled ‘Bell state’ that also depends on  $\theta$ ,  $|Bell(\theta)\rangle$ . Finally, quantum state tomography is performed on  $|Bell(\theta)\rangle$ .



**Figure 2.6:** (a) and (b) are the plots of the measured negativities after applying QREM at different Z-rotation angles in the preparation of the Bell state on qubit pair 383-384 of the device *ibm\_seattle* and qubit pair 8-9 of the device *ibm\_cairo* respectively. Red lines are the unmitigated negativities, and blue lines are the mitigated ones measured in four trials, where light colours represent each trial. Error bars are therefore the 95% confidence level calculated from 1.96 times the standard error. The shaded region above the curve  $\frac{1}{2} \sin \frac{\theta}{2}$  is theoretically forbidden since the curve is the ideal negativity.

In Figure 2.6a, we plot the average negativity versus rotation angle  $\theta$ . The mitigated negativity falls below the theoretical value most of the time. This strongly indicates that even for non-perfect entanglement with analytical negativity  $< 0.5$ , QREM is not over-correcting into the shaded region. Although we notice for  $\theta < \frac{\pi}{3}$ , the negativity after filtering out readout errors exceeds the theoretical value, which could be explained by the revealing of crosstalks used to be overwhelmed by readout noises. Since such behaviour only occurs at small rotation angles and thus weak entanglement, it is confident to say that at  $\theta > \frac{\pi}{3}$ , generation of entanglement is still dominated by preparation of Bell state itself and mitigated negativities are not exceeding the expectations. Also, by applying the same procedures on a qubit pair of another device

*ibm\_cairo* (Figure 2.6b), which also produces relatively high improvements in negativity, we observe that almost all mitigated negativities falls below the analytical curve, except at  $\theta = 0$  which is likely due to the same problem of the crosstalks.

After conducting the tests on the validity of QREM, we evaluate the usage of QREM on negativity mitigation of our work to be feasible and is not producing improvements more than it should. As long as the initial entanglement of the Bell state is set to be strong, it is safe to conclude that negativity contribution is dominated by the gates rather than by correlated noises, and mitigated negativities do not exceed the theoretical value.

## 2.3 Characterisation of Multi-Partite Entangled States

Since physicists have viable access to NISQ quantum devices, searching for GME in large entangled states has become an intense race. Works done from different groups [24, 34, 53] have advanced the generation of GME up to a system of 51 qubits. In this section, we compare the traditional strategy of fidelity estimation using full QST against fidelity estimation using randomised stabilisers first introduced by [44]. By comparing the fidelities measured from a 6-qubit graph state using those two methods, we show that the computational resources required for randomised stabilisers are much more reachable than full QST with minimal sacrifice on statistical uncertainties. Also, we successfully demonstrate the GME on graph states up to 14 qubits on an IBM Quantum device using randomised stabilisers under limited resources.

### 2.3.1 Fidelity Estimation Using Randomised Stabilisers

As previously discussed in Section 1.4.4, to calculate the fidelity of a state, one must obtain the corresponding noisy state density matrix. Such criterion is time unfriendly because the order of complexity is exponential for ordinary QST. Therefore, it is necessary to develop new algorithms that make the calculation of fidelity scalable. As a modification of full QST, randomised fidelity estimation [44] utilises a special property of vanishing expected value on non-stabiliser Pauli string observables of graph states. In general, we can write the formula of the fidelity between our ideal pure state  $\rho$  and noisy state  $\zeta$  as

$$F(\rho, \zeta) = \text{tr}(\rho\zeta) = \sum_k \chi_\rho(k)\chi_\zeta(k), \quad (2.2)$$

where  $\chi_\rho(k) = \text{tr}(\rho W_k / \sqrt{d})$  is the normalised expected value of the Pauli string  $W_k = \sigma_{k_1} \otimes \sigma_{k_2} \otimes \dots \otimes \sigma_{k_{\log_2(d)}}$  with label  $k$  with respect to the state  $\rho$ ,  $k \in \{1, 2, \dots, d^2\}$  and  $d$  is the dimension of the hilbert space  $\rho$  lives in.

Luckily, for stabiliser states,  $\chi_\rho(k)$  is only non-zero if  $W_k$  belongs to one of the  $d$  stabilisers. Therefore, instead of measuring the expected value of all possible  $n$ -fold Pauli-operator tensor products of a  $n$ -qubit state, it only picks  $1/d$  portion of all Pauli strings to measure, such that the total number of circuits required is drastically reduced by a factor of  $d$  [44]. Specifically,

for well-conditioned states such as graph state, in which its generators are defined as in Section 1.4.1, it is explicit that  $\chi_\rho(k) = 1$  or  $0$  if  $W_k$  is a stabiliser or not. Hence, the *actual* fidelity is equivalent to  $\sum_k \sum_{j \in S} \chi_\zeta(k) \delta_{k,j}$ , where  $S$  is the set of labels for stabilisers. Therefore, only  $\chi_\zeta(k)$  with  $k$  coincident with a stabiliser needs to be sampled. Also, considering the conservative estimate of the sampling error probability  $\delta$  outlined in [44], the probability of the measured fidelity deviates from the actual fidelity by  $\epsilon$  less than  $\delta$  is given by the Hoeffding's inequality,

$$P(|\bar{F} - F| \geq \epsilon) \leq \delta = 2 \exp\left(-2\epsilon^2 / \sum_{i=1}^l (b_i - a_i)^2\right), \quad (2.3)$$

where  $F$  is the actual fidelity and  $\bar{F} = \frac{1}{l} \sum_{i=1}^l \chi_\zeta(k=i)$  is the measured fidelity only sampling from  $l$  stabilisers. In our case of graph states, assuming there is no chance of obtaining a negative expected value, we let  $a_i=0$ ,  $b_i = 1/l$  be the lower and upper bound of the random variable  $\chi_\zeta/l$  can take. After rearranging, the number of measurement circuits to estimate the fidelity would be only dependent on the confidence level additive error  $\epsilon$  and probability of failing  $\delta$ , meaning that the number of circuits required can be further reduced to constant with respect to the number of qubits once fixing  $\epsilon$  and  $\delta$ ,

$$l = O\left(\frac{\log(1/\delta)}{\epsilon^2}\right). \quad (2.4)$$

Depending on how much trade-off between time complexity and tolerance to statistical errors is needed, one can freely set the number of stabilisers  $l$  required from their desired confidence level and errors or vice versa. Since  $l$  is independent of the number of qubits in the state, this method gives considerable benefits in scaling up the realisation of GME. Next, we will show the results obtained from applying such a technique.

### 2.3.2 Fidelity Estimation Realisations on IBM Quantum Devices

On a 6-qubit graph state prepared on *ibmq\_jakarta*, we calculate the fidelity measured using both full QST and randomised stabilisers with the aid of Algorithm 1 to reconstruct physical probability vectors and density matrices. By selecting 64 stabilisers randomly and executing 1000 shots on each stabiliser that is repeated in 4 trials, the estimated fidelity is found to be  $0.943 \pm 0.085$  where the uncertainty is determined from  $\epsilon/\sqrt{4}$  corresponds to 95% confidence level where  $\delta = 0.05$ . On the other hand, the full QST takes a total of 729 Pauli string operators per trial and is also repeated in 4 trials. We find that the fidelity is  $0.926 \pm 0.0272$ , where the uncertainty is also calculated in the same way that corresponds to 95% confidence level. Colourmaps of the reconstructed density matrix of the 6-qubit graph state, as well as the corresponding analytical solution, both norm and phase, are shown in Figure 2.7 and 2.8. From the colourmaps, despite slight fluctuations in the amplitude of matrix elements and small rotations on overall phases, the state we prepared is of high quality and high fidelity. By comparing the results from full QST and randomised stabilisers, it is clear that the fidelity obtained from full QST falls into the 95% confidence interval of the fidelity determined from 64 stabilisers. In other words, if we assume the full QST fidelity is the *actual* fidelity, it is evident

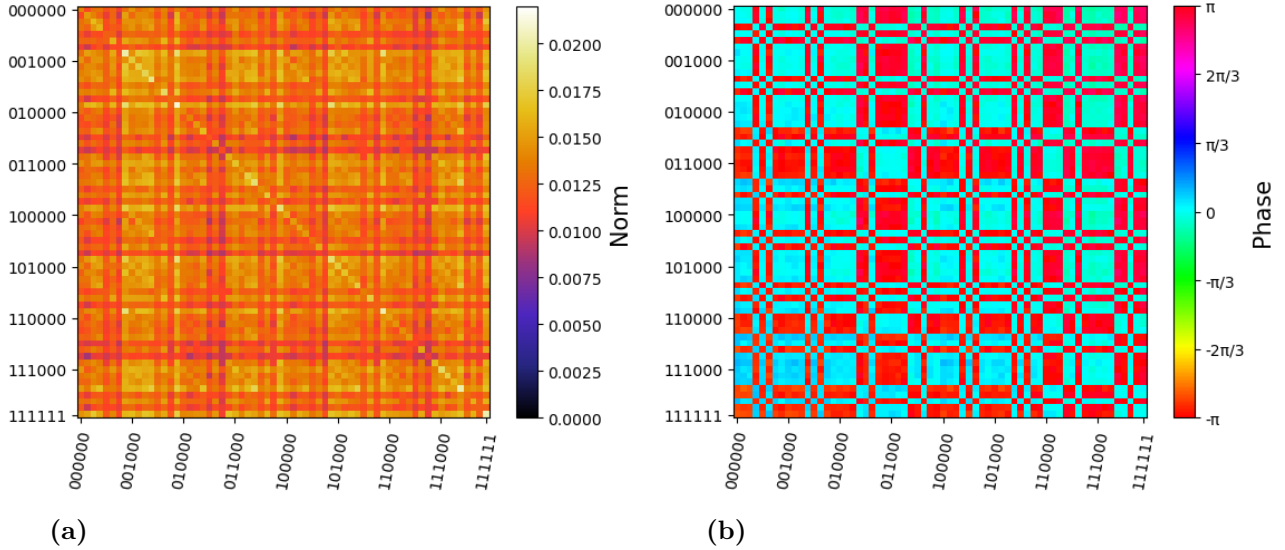


**Figure 2.7:** Colourmaps of (a) Norm and (b) phase of the 6-qubit graph state from the density matrix prepared on IBM Quantum device *ibmq\_jakarta*. The value of each element in the matrix has its colour on the map represented. For the norms, the more bright the colour is, the higher its value; cyclic colourmaps are used for the phases.

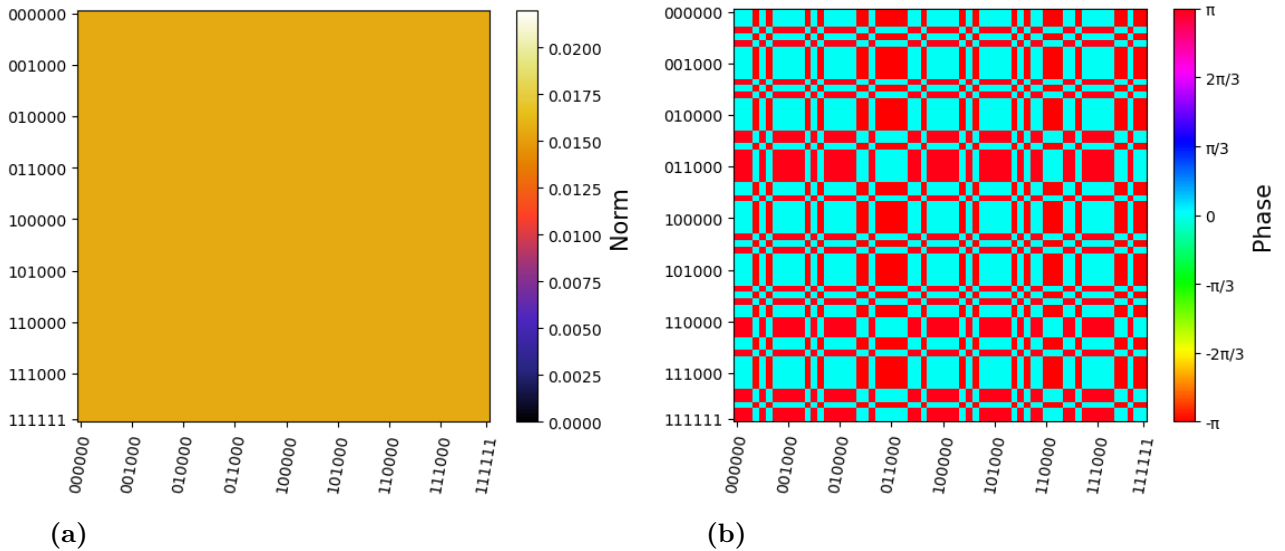


**Figure 2.8:** Colourmaps of (a) Norm and (b) phase component of the *ideal* 6-qubit graph state density matrix without noise that has the same topology as the above.

that predictions about the error range made in [44] are correct. We can safely conclude that fidelity obtained using randomised stabilisers can be used to infer the actual fidelity.

Under a restricted number of circuits, we also calculated fidelities using randomised stabilisers up to 14 qubits. Figure 2.9 plots the fidelities of graph states prepared on the device *ibm\_cairo* from 7 to 14 qubits. Each is computed from 512 random stabilisers, except for the 7 and 8-qubit case, only 128 and 256 stabilisers are available. At the same time, we also carry out Algorithm 2 to avoid possible negative probability after QREM.

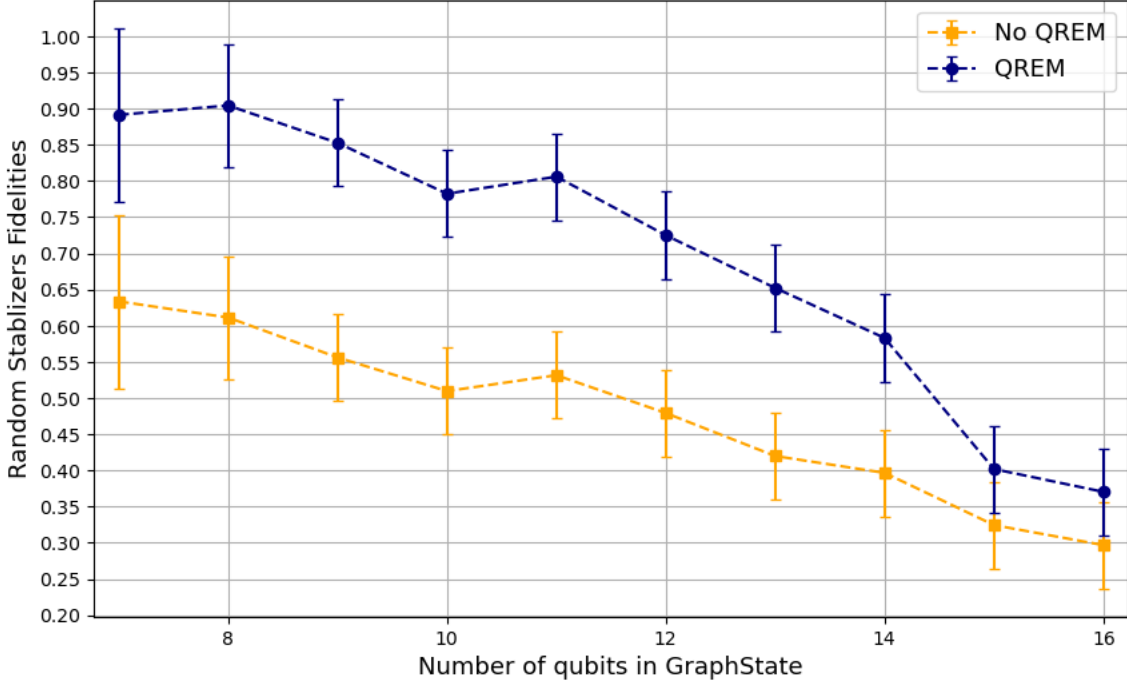


**Figure 2.9:** Fidelities calculated using randomised stabilisers versus the number of qubits in graph state prepared on *ibm\_cairo*. Each graph state randomly selects 512 stabilisers (except for 7 and 8-qubit graph states, only 128 and 256 stabilisers are available) and each stabiliser circuit is executed in 5000 shots.

When the size of graph states are smaller or equal to 14 qubits, the 95% confidence interval of the fidelities after applying QREM is found to be above the 0.5 thresholds of GME recognition. Therefore, assuming reasonable estimations of actual fidelities, we produce graph states that are proved to be GME up to 14 qubits. Yet, unlike what was done in [24], which took  $4.3992 \times 10^8$  shots to verify a 51-qubit graph state, because only a small number of stabilisers are selected to estimate the fidelities in our practice, there is still room to improve from such results. Also, considering the existence of errors other than bit-flip errors, such as decoherence and cross-talks, it is reasonable to expect that GME can be demonstrated on a larger prepared graph state once those errors can be mitigated.

## 2.4 Hamiltonian Moments as an Entanglement Estimation Algorithm

To tackle the problem of inefficiency and non-scalability in full Quantum State Tomography for large-scale quantum states, we seek other scalable methods of determining the quality of entanglement on large states. By taking advantage of quantum computed moments recently introduced for the computation of ground state energies for trial states in Variational Quantum Eigensolver (VQE) [51, 54], we develop a new tool for measuring the entanglement of large noisy graph states by calculating how far their energy is to the ideal ground state with respect to the chosen Hamiltonian.

In our method, we first construct a unique Hamiltonian such that the ideal graph states are the only ground states. Then, we prove that the method of Hamiltonian moments has a cost complexity of logarithmic order  $O(\log(N^p))$  in quantum computation time, and polynomial order  $O(N^p)$  in classical post-processing time, where  $N$  is the number of qubits in the graph state and  $p$  is the highest order of the moments. Compared to using full QST (which requires  $O(3^N)$  measurements) to estimate entanglement, this is an exponential improvement both in the quantum and classical computation time with respect to the number of qubits. Next, utilising such a superiority in time complexity, we demonstrate the scalability and validity of this method in characterising entanglement by measuring the energies of prepared graph states up to 127 qubits for the first time. We also show a solid correlation to the actual fidelities to increase the credibility of this method. Moreover, by comparing the amount of correction made from the first moments to the final energies, we understand the behaviour of graph states moving close to one of the Hamiltonian eigenstates as more qubits are involved.

### 2.4.1 Energy Estimation using Hamiltonian Moments

As a technique for calculating corrected energy to a quantum state with respect to a selected Hamiltonian, Hamiltonian moments are often used for obtaining a higher order correction to the energy obtained in VQE [51, 54]. However, it could also be viewed as another way to efficiently and directly characterise the whole quantum state. Instead of directly computing the fidelity with respect to the desired state, this method focuses on evaluating the energy of the prepared state and thus hints at how close it is to the ideal state. Details of this algorithm will be discussed here and in later subsections.

To estimate the *actual* energy of the noisy state, one must define a Hamiltonian such that the desired *ideal* state is the ground state. Established on such a Hamiltonian, this method utilises the Lanczos Method [55] of diagonalizing the Hamiltonian to approach the ground state energy. By first recursively generating a new trial state with respect to the graph state Hamiltonian, we can write

$$|v_n\rangle = \frac{1}{\beta_{n-1}} [(H - \alpha_{n-1}) |v_{n-1}\rangle - \beta_{n-2} |v_{n-2}\rangle], \quad (2.5)$$

where  $\alpha_n = \langle v_n | H | v_n \rangle$ ,  $\beta_n = \langle v_{n+1} | H | v_n \rangle$  are the Lanczos coefficients of the tri-diagonal hamiltonian in a new basis. They can be reverse-engineered from cumulants of the Hamiltonian of the base trial state. For large  $n$  and system size  $N$ , a cluster expansion can be defined [54],

$$\alpha(z) = c_1 + z \left( \frac{c_3}{c_2} \right) + z^2 \left( \frac{3c_3^3 - 4c_2c_3c_4 + c_2^2c_5}{4c_2^4} \right) + O(z^3) \quad (2.6)$$

$$\beta^2(z) = zc_2 + z^2 \left( \frac{c_2c_4 - c_3^2}{2c_2^2} \right) + O(z^3) \quad (2.7)$$

where the cumulants are obtained from moments  $\langle H^n \rangle$ ,

$$c_n = \langle H^n \rangle - \sum_{p=0}^{n-2} \binom{n-1}{p} c_{p+1} \langle H^{n-1-p} \rangle. \quad (2.8)$$

The parameter  $z = \lim_{n,N \rightarrow \infty} O\left(\frac{n}{N}\right)$  is a positive parameter obtained when both number of trial states iterations  $n$  and size of the system  $N$  goes to infinity. Therefore, the kernels of the characteristic polynomial of  $T_n$  with respect to  $H$  in terms of the Lanczos coefficients can be used to express the ground state energy [54],

$$E_0^{\text{inf}} = \inf [\alpha(z) - 2\beta(z)]. \quad (2.9)$$

In the first order of  $z$ , the ground state energy can be approximated by differentiating  $E_0^{\text{inf}}$  with respect to  $z$  and equating to 0 [54]. For moments and cumulants up to order  $n = 4$ , this is explicitly

$$E_0^{\text{inf}} = c_1 - \frac{c_2^2}{c_3^2 - c_2 c_4} \left[ \sqrt{3c_3^2 - 2c_2 c_4} - c_3 \right]. \quad (2.10)$$

We denote the value of  $z$  such that ground state energy is minimised as  $z = z^*$  [56].

$$z^* = \frac{c_2^3 (\delta - c_3 \sqrt{\delta})}{\delta (c_3^2 - c_2 c_4)} \quad (2.11)$$

where  $\delta = 3c_3^2 - 2c_2 c_4$ .

By finding the ratio of the initial guess  $c_1$  to the corrected energy  $E_0$ , this value can be used to quantify how close the prepared state is to its nearest eigenstate of  $H$ . Explicitly this ratio is written as

$$\frac{c_1}{E_0} = 1 - \frac{z^* \sqrt{\delta}}{c_1 c_2}. \quad (2.12)$$

### 2.4.2 Graph State as an Eigenstate of The Hamiltonian

In order to implement moments methods of entanglement estimation by calculating energies, we construct special Hamiltonians such that the ideal graph states are the unique ground states for each of those Hamiltonians. Inspired by the idea that the generator of stabilisers uniquely defines a specific quantum state, we construct the graph state Hamiltonian from the graph state stabiliser generators. As introduced in Section 1.4.1, each of the generators  $K_\alpha$  has an eigenvalue of +1 when acting on the graph state  $|\phi(G)\rangle$  defined on a graph  $G$ . Therefore, with respect to a graph  $G$ , we define the Hamiltonian to be

$$H = \frac{-1}{|V(G)|} \sum_{\alpha \in v(G)} K_\alpha, \quad (2.13)$$

where  $K_\alpha$  is a generator of the stabilisers defined on vertex  $\alpha$ . In such a way, the definition of the Hamiltonian ensures  $|\phi(G)\rangle$  has the lowest possible energy of  $-1$ ,  $H |\phi(G)\rangle = -|\phi(G)\rangle$ . It is also the fact that this set of stabilizers uniquely defines a graph state such that it is impossible to return an eigenvalue of +1 when acting each  $K_\alpha$  on some other states  $|\psi\rangle$  which are not the native graph state. This ensures  $|\phi(G)\rangle$  is the only ground state with respect to  $H$ . However, we will demonstrate that further optimisations are still possible in the next section.

### 2.4.3 Complexity Suppression Using Tensor Product Basis Sets

To compute the expected values of Hamiltonian moments  $\langle H^n \rangle$  with order  $n$ , one must know the expected value for each of its terms. Therefore, to reduce the number of Pauli string terms that need to be measured, Tensor Product Basis (TPB) sets developed in [51] are used to group Pauli strings. The key idea of constructing a TPB set is to find a group of Pauli strings to induce a special Pauli string that is qubit-wise commuting to the rest of the group. Therefore, the expected values of all the Pauli strings in the group can be found through the bit-string counts obtained from basis measurement shots of that particular string by simply ignoring the sites that represent identities. We consider the terms in the expansion of a Hamiltonian moment as

$$H^n = \left( \sum_i w_i P_i \right)^n = \sum_j A_j^{(n)} P_j^{(n)}, \quad (2.14)$$

where  $w_i$  and  $P_i$  are the coefficients and Pauli string of each term in the Hamiltonian respectively.  $A_j^{(k)}$  are the coefficients of each expanded Pauli string  $P_j^{(n)}$ . This in principle grows the number of terms and hence the number of circuits to calculate their expected values polynomially  $O(N^p)$ , where  $N$  is the number of qubits and  $p$  is the highest power of the moments. To avoid this, we group all Pauli strings observables into TPB sets such that only one observable from each set is needed to find the expected value,

$$\{P_j^{(n)}\} \Rightarrow \{S_1, S_2, \dots, S_m\}, \quad (2.15)$$

where each  $S_k \subseteq \{P_j^{(n)}\}$  is a set of TPB Pauli strings. Within each set  $S_k$ , every Pauli string  $\{S_k\}_i$  is qubit-wise commuting (QWC) to others, such that  $[\{S_k\}_{a_j}, \{S_k\}_{b_j}] = 0$  for all  $a, b$  at site  $j$ . The Pauli string  $Q_k$  is induced from  $S_k$  by taking the common non-identity operator (if there is any) on the site  $j$  over every  $\{S_k\}_i$  to represent  $Q_{k_j}$ . Therefore, every Pauli-operator in  $\{S_k\}_i$  is either the same as the Pauli-operator in  $Q_k$  for the same site or is the identity.

By exploiting this idea, we develop Algorithm 3 that outlines details of constructing TPB sets from scratch. In practice, since the measurement results from identities are ignored in the calculation of expected values, the expected values of all Pauli strings in  $S_k$  can be derived from only the bit-string counts from measuring the  $Q_k$  basis. Also, we find that the time cost in quantum computation is drastically reduced to logarithmic order. In Figure 2.10, we analyse the number of TPB sets generated according to Algorithm 3 on graph states prepared on IBM Quantum devices with same heavy-hexagonal lattice structure. Up to different highest orders of Hamiltonian moments, we plot the number of TPB sets against  $N^p$ , the number of qubits raised to the power of highest order  $p$ . It is obvious that for various  $p$  between 2 and 5, the number of TPB sets fits very closely to the function  $f(N) = a \log(N^p) + b$ , indicating strong evidence that the number of quantum circuits required grows just logarithmically to the number of qubits in graph state. However, it is to be noted that the cost of time in classical post-processing to reconstruct all expected values still scales polynomially.

In comparison, the full QST grows exponentially in computing resources:  $O(M3^N)$ , where  $N$  is the number of qubits and  $M \sim N/\varepsilon^2$  is the statistical correction factor accounts for the approximation to be within error of  $\varepsilon$  to the actual value and with probability of success close to 1 [57]. Even with improved version [58], it only reduces the complexity down to  $O(2^N N^2)$ .

---

**Algorithm 3** An algorithm that finds all TPB sets from a list of Pauli strings and puts the Pauli string with the least identities at first in each of the sets

---

**Input:** Pauli strings  $\{P_j^{(n)}\}$ ,  $|\{P_j^{(n)}\}| = M$

**Output:** Tensor product basis sets  $T = \{S_1, S_2, \dots, S_m\}$ ,  $S_k = \{Q_k, \dots\}$ ,  $m \ll M$

- 1: Let  $S_1 = \{Q_1 = P_1^{(n)}\}$ ,  $T = \{S_1\}$ ,  $m = 1$
- 2: **for**  $j = 1, 2, \dots, M$  **do**:
- 3:     **for**  $i = 1, 2 \dots, |T|$  **do**:
- 4:         BWC  $\leftarrow$  True
- 5:         **if**  $P_j^{(n)}$  is not BWC with  $Q_i$  **then**:
- 6:             BWC  $\leftarrow$  False
- 7:         **end if**
- 8:         **if** BWC is True **then**:
- 9:             Add  $P_j^{(n)}$  to  $S_i$
- 10:          **for**  $k = 1, 2 \dots, \text{len}(Q_i)$  **do**:
- 11:             update  $Q_{i,k} \leftarrow Q_{i,k} \delta(Q_{i,k}, P_{j_k}^{(n)}) + Q_{i,k} P_{j_k}^{(n)} (1 - \delta(Q_{i,k}, P_{j_k}^{(n)}))$ .
- 12:          **end for**
- 13:          **break**
- 14:         **end if**
- 15:     **end for**
- 16:     **if** BWC is False **then**:
- 17:          $T \leftarrow T \cup S_{m+1}$ ,  $S_{m+1} = \{Q_{m+1} = P_j^{(n)}\}$
- 18:          $m \leftarrow m + 1$
- 19:     **end if**
- 20: **end for**
- 21: Output  $T$

---

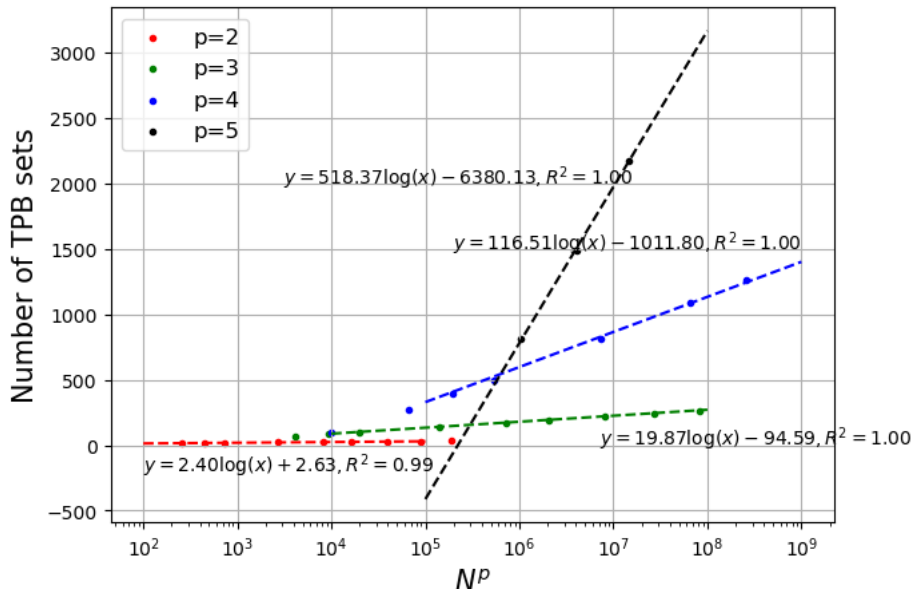


**Figure 2.10:** Plots of number of TPB sets versus  $N^p$ . Note that the horizontal axis is plotted in logarithmic scale with  $R^2 \approx 1$ , articulating the fact that the time cost in quantum computation is indeed in  $O(\log(N^p))$

There are even methods of reconstructing a full density matrix by avoiding performing full QST [59, 60] which has achieved convergence of calculated fidelity on a 20-qubit quantum state. It is claimed that this can reduce the number of circuits to  $O(\text{poly}(N))$ , but sacrifices either short circuit depth or requires obtaining reduced density matrices to reconstruct the full density matrix. Even for the randomised stabilisers, the required measurements are still worth questioning [24]. On the other hand, by ignoring the density matrix, the moment method uses the ground state energy as a metric to approximate how well the state is prepared, such that the number of measurements is significantly reduced from exponential to sub-logarithmic scale.

#### 2.4.4 Ground State Energies

We follow the procedures just introduced in Section 2.4.1, 2.4.2, 2.4.3 to measure the energies of graph states with the highest order of moments up to four prepared on the IBM Quantum device *ibm\_brisbane*. Similar to the fidelity estimation, Algorithm 2 of physical probability vectors calculation is also applied before evaluating the moments. In Figure 2.11, we plot the energy of graph states in different numbers of qubits up to 127 against the estimated net error of the coupling gates. Similar to our definition of readout net error in Section 2.1, we define the net coupling error as the one minus the product of all two-qubit coupling gate fidelities involved in the construction of a specific graph state,

$$\epsilon_{\text{net}} = 1 - \prod_{i \in E(G)} (1 - \epsilon_i), \quad (2.16)$$

where  $i$  is the label of the edges that are incident to two qubits of the graph state.

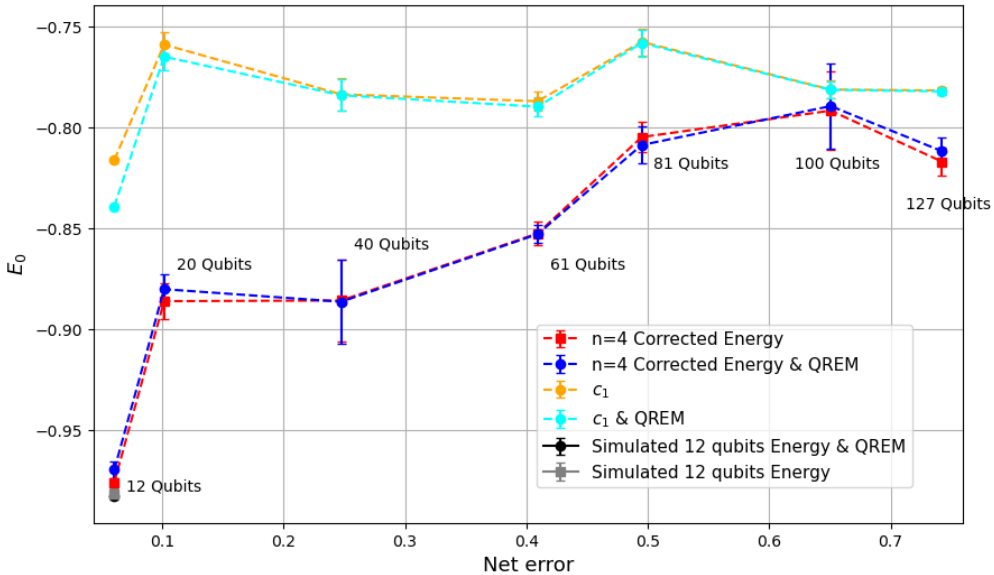


**Figure 2.11:** Plot of the estimated energy ( $E_0$ ) of graph states from 12 to 127 qubits to the fourth order of correction in moments, versus the coupling gate net error. The blue and red bars represent the calculations with and without QREM on the energies. Orange and light blue bars are the energy calculated from just the first moment/cumulant. Grey and black dots are put in for reference for energies calculated from simulations of circuits.

In our design, the ideal ground-state energy of those graph states is set to be  $-1$ . Naturally, a straightforward standard of judging how well those graph states are prepared is by looking at how far their estimated energies are from the ideal cases. Because the overall entanglement becomes more fragile as the number of qubits increases, we expect the measured energies to be far from the ideal case when more qubits are involved. In our experiment, on average the measured energies of the graph states increase as the number of qubits increases or as the net error increases. To draw a comparison, we also include the energy measured from a 12-qubit graph state that is classically simulated. Because of the small difference in actual measurement  $E_0 = -0.970 \pm 0.004$  versus simulation  $E_0 = -0.982 \pm 0.001$ , we highlight that our approximation is close with only 1.2% difference, and the measurement of the energies nicely captures the actual situation.

On top of that, the calculation for the 127-qubit graph state takes a total of 1263 TPB sets, which includes 10,676,129 Hamiltonian moment terms. On average, this requires 78 minutes of system time to execute on the IBM quantum device *ibm\_brisbane* and 2711 minutes on the NCI high-performance supercomputer *Gadi* for post-processing per trial. Thanks to its embarrassingly parallel nature [61] when calculating the moments from every count, the classical post-processing is performed in perfect parallel by accessing 12 cores of Intel Xeon Platinum 8470Q (Sapphire Rapids) 2.1 GHz CPUs in *Gadi*. By accessing *Gadi*, the total time required for computation is drastically suppressed, allowing us to finish the calculation of energies of graph state up to 127 qubits promptly. Although the time cost in classical computation still scales polynomially in  $O(N^4)$ , we emphasise that TPB sets drastically reduce the time cost in quantum computation, which is a more scarce resource, down to  $O(\log(N^4))$ .

Moreover, combined with the fidelities previously obtained from randomised stabilisers, Figure 2.12 demonstrates a very strong negative correlation ( $-0.967$ ) between the measured fidelity and energies. Therefore, to a high confidence level, the energies estimated using Hamiltonian moments can reflect the fidelity of graph states and hence the quality of its entanglement.

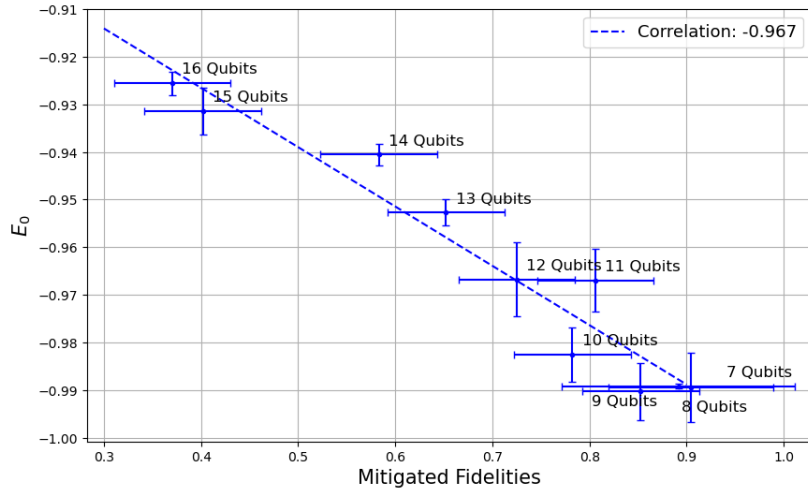


**Figure 2.12:** Plot of the correlations between the estimated energies using moments and fidelities estimated using randomised stabilisers with experiments performed on *ibm\_cairo* previously shown in 2.9. Data shown in both axes are mitigated using QREM. Two times the standard error of the mean sampled in four trials are used in vertical error bars, and horizontal error bars are the same as in 2.9

### 2.4.5 Distance to Nearest Eigenstate

From another perspective, we observe that the first cumulant  $c_1 = \langle H \rangle$  as in equation 2.8 converge to the final estimation of the energy as the number of qubits or net error increases. By making use of equation 2.12, we plot the values of  $c_1/E_0$  in Figure 2.13. It is a clear trend that  $c_1/E_0$  is approaching one as the net error increases. According to our interpretation of the equation, the more  $c_1/E_0$  is close to one, the more likely the noisy graph state is closer to one of the Hamiltonian eigenstates. This is because if the correction made to the first-order estimation  $c_1$  to obtain the fourth-order estimation  $E_0$  is small, the state should be closer to the nearest Hamiltonian eigenstate where the distribution of sampled  $\langle H \rangle$  is sharp and symmetric. Unfortunately, the Hamiltonian eigenstate is not necessarily the ground state.

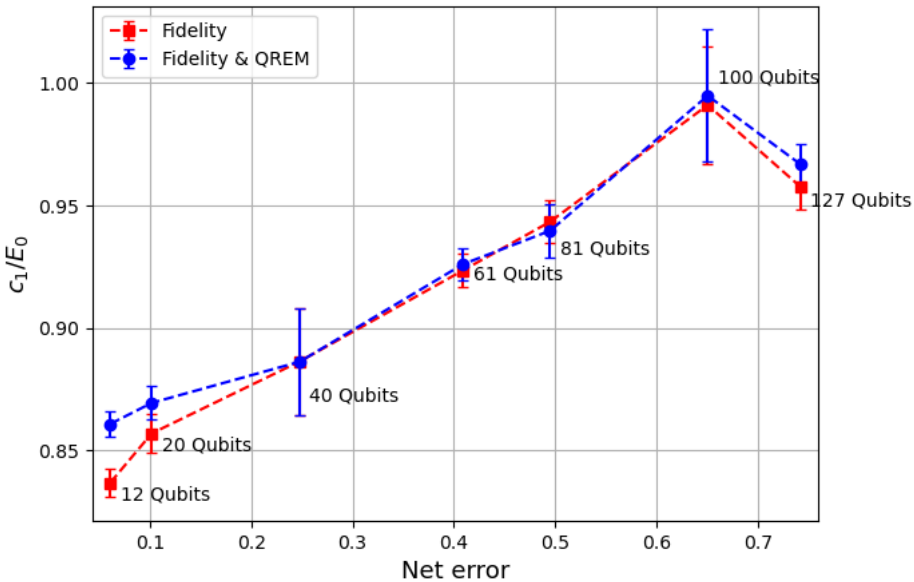


**Figure 2.13:** Plot of  $c_1/E_0$  versus coupling gate net errors. The red and blue bars indicate the numbers calculated from unmitigated and mitigated data with QREM respectively. Error bars take two standard errors sampled in 8 trials. The value of  $c_1/E_0$  marks the significance of how close the noisy graph state is to one of the eigenstates in the Hamiltonian.

In this specific case, a possible reason that explains this trend is that a graph state Hamiltonian has dimension  $2^N \times 2^N$ , which therefore has the number of its eigenvalues/eigenstates in  $O(2^N)$ , where  $N$  is the number of qubits. However, since eigenvalues are strictly bounded by  $[-1, 1]$  regardless of  $N$ , it is easier for the prepared state to have its energy close to one of the eigenvalues as they become denser within the range. On the other hand, being close to an eigenstate is not equivalent to being close to the ground state, especially when they are dense. Therefore, further research is needed to evaluate the mechanism of higher-order moment corrections.

Nevertheless, our research shows that the moment method of energy estimation could become a time-efficient way of evaluating the quality of entanglement on graph states. Although this is unable to measure the fidelity of a given state, it indirectly provides a strong negative correlation between the estimated energies and the fidelities of prepared states, which are shown to be scalable.

# 3 Entanglement Preservation of Graph States

## 3.1 Introduction

Apart from characterising the entanglement of quantum states immediately after they are created, a key research topic is to find ways to sustain the entanglement between qubits as long as possible. Unlike classical computers which store data in microscopic capacitors that are highly stable and could easily last for years, quantum states are hard to preserve subject to inevitable interactions with the environment, which can only sustain less than a minute [62]. Especially for the superconducting qubits architecture of quantum computers such as the IBM quantum devices, fast decoherence time of  $O(10^2)$   $\mu\text{s}$  for a single qubit is one of the major concerns restricting its performance in large-depth circuits [63].

Work has been done since the last decade to improve the stability of quantum states prepared. This includes the building of new architectures of qubits memory such as encoding qubits in electron-nuclear couplings [64], charge noise suppression [65], as well as externally intervene strategies like dynamical decoupling [66, 67] that suppresses the decoherence of qubits by cancel or decouple the idle rotations of qubit state vector on Bloch sphere, hence lengthen its lifetime.

In this chapter, we extend the technique of dynamical decoupling [66, 67] and double  $\pi$ -pulses [68] onto a 5-qubit graph state prepared on *ibmq\_manila*. By showing more than doubling in its characteristic lifetime compared to the case of natural delay using dynamical decoupling, we demonstrate the efficacy and efficiency of such a method in preserving entanglement. We also anticipate this method is also scalable to large-entangled states. Source codes for this program are available under [https://github.com/KangHaiYue/MSc\\_Project/blob/main/main%20project/graphstate.py](https://github.com/KangHaiYue/MSc_Project/blob/main/main%20project/graphstate.py).

### 3.1.1 Periodic Dynamical Decoupling

The underlying principle of Periodic Dynamical Decoupling (PDD) originates from [68] that was first implemented in the application of Nuclear Magnetic Resonance. The fundamental idea is to cancel idle precessions of the quantum spins in the magnetic field about some axis by periodically flipping their moments [66, 67], hence stabilizing the spins. In the practice of quantum computation, rapid control pulses such as  $\pi$ -pulses are applied periodically onto a circuit to suppress errors caused by idle rotations, where a  $\pi$ -pulse stands for rotation in  $X$ -axis of the Bloch sphere of a qubit by angle of  $\pi$ . Such a technique aims to “decouple” the local static Hamiltonian of the system itself as much as possible from the total Hamiltonian, which contains interaction terms with the environment. For example, a system  $S$  of one qubit coupled to an environment reservoir  $R$  defined on the Hilbert space  $\mathcal{H} = \mathcal{H}_S \otimes \mathcal{H}_R$  has the total Hamiltonian in the form of local Hamiltonian plus the interaction term,

$$H_0 = H_S \otimes I + I \otimes H_R + H_{SR}, \quad (3.1)$$

where  $H_S, H_R$  are locally non-interacting Hamiltonian and  $H_{SR} = f(H_S \otimes H_R)$  is the interaction Hamiltonian with eigenvalues conditionally depends on both eigenstates of  $H_S$  and  $H_R$ . The evolution of the system  $S$  is not yet decoupled from its environment, which will cause idle rotation in the phases. To protect the evolution of  $S$  from the interaction  $H_{SR}$ ,  $\pi$ -pulses of negligible widths are acting in a constant frequency on  $\mathcal{H}_S$ , which produces a time-dependent Hamiltonian  $H(t) = H_0 + H_1(t)_S \otimes I_R$  and the corresponding unitary propagator,

$$U(t) = \exp \left\{ -i \int_0^t dt' H(t') \right\} = \left( X \otimes I \exp \left( \frac{-it}{2n} H_0 \right) X \otimes I \exp \left( \frac{-it}{2n} H_0 \right) \right)^n \quad (3.2)$$

where  $2n$  is the number of  $\pi$ -pulses within the total time of delay  $t$  and  $X$  is acted on  $\mathcal{H}_S$  only. By consecutively applying  $X$  gates and taking the Trotter limit when  $n \rightarrow \infty$ , we obtain an effective time-independent Hamiltonian  $H_{\text{eff}} = (X \otimes I)H_0(X \otimes I) + H_0$ , which is closer to  $H_S \otimes I + I \otimes H_R$  compared to the original  $H_0$ . In case when  $H_{\text{eff}} \rightarrow H_S \otimes I + I \otimes H_R$ , the evolution of the state on  $s$  is totally decoupled with the environment, hence obtaining  $|\psi_{\text{tot}}(t)\rangle = |\psi_S(t)\rangle \otimes |\psi_R(t)\rangle$  [66].

In order to carry this out in practice and examine the decoherence of graph state with or without dynamical decoupling, the quantum circuits are built as in Figure 3.1 by [32]. By inserting several parallel  $X$  gates inside a period of delay of time  $t$ , it divides the delay into sections with lengths in the ratio of  $1 : 2 : 2 \dots : 2 : 1$ . In this way, the total delay time with the odd labels is equal to the total delay time with the even labels,  $\sum_{i=\text{odd}} \text{Delay}_i = \sum_{j=\text{even}} \text{Delay}_j$ .

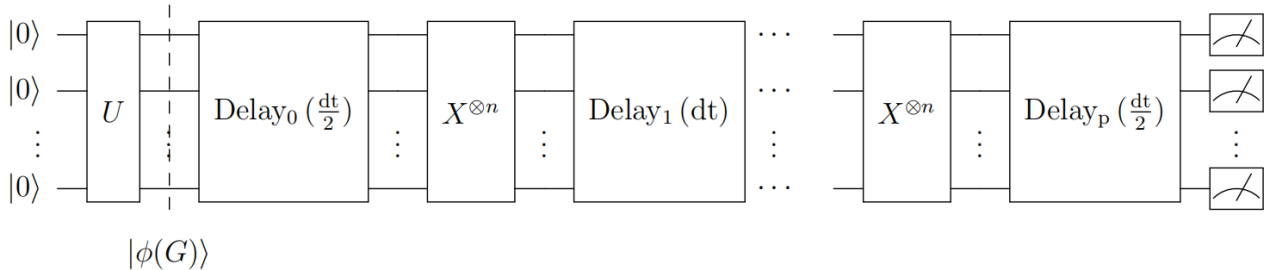


**Figure 3.1:** The periodic dynamical decoupling circuit in practice. Gate  $U$  generalises the circuits to build a given graph state  $|\phi(G)\rangle$ . A total of  $p$  sets of parallel  $X$  gates are distributed in the circuit, separating the delays into  $p + 1$  sections with labels from 0 to  $p$ . Delays between pulses of length  $dt$  sum up to total delay time  $t$ .

Therefore, any idle precessions of state in the  $X$ -direction will alternate back and forth with total time in a clockwise direction equal to the total time in an anti-clockwise direction. In principle, the net effect of the precession in  $X$ -direction is zero. In the case of graph states, since they are not eigenstates of  $X^{\otimes n}$ , the total number of layers of  $X$  gates are in multiple of two such that the graph state remains unchanged before measurement. Similarly, Figure 3.2 demonstrates the circuit of a naturally delaying state without any dynamical decoupling or entanglement preservation techniques, where the state is measured directly after a time delay  $t$ . In the next section, the entanglement obtained from dynamical decoupling and natural delay will be compared regarding their average decoherence time in fidelity and the significance of such technique in entanglement preservation.

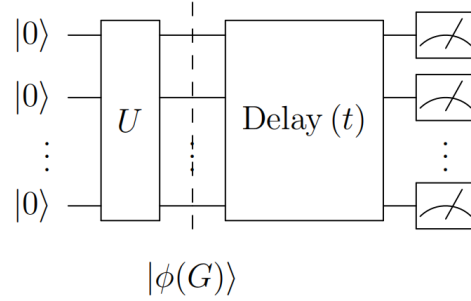


**Figure 3.2:** Circuit diagram of the free delay of the graph state without any dynamical decoupling measures. Gate  $U$  generalises the circuits to build a given graph state  $|\phi(G)\rangle$ . The delay gate works by pausing the circuit by total time  $t$  before measuring the results.

## 3.2 Extending Graph State Coherence Time

### 3.2.1 Improvement of coherence time

After implementing the technique of dynamical decoupling as explained in equation 3.1, 3.2, we obtain the fidelities of a 5-qubit graph state generated on *ibmq\_manila* using QST previously introduced in Section 1.4.2. Similar to previous works, Algorithm 1 and Algorithm 2 that evaluates physical probabilities and density matrices respectively are also applied. By trialing total delay times starting from 0 to 15  $\mu\text{s}$  and different layers of  $X$  gates, we observe the fidelity decay with respect to time as expected. Specifically, we compare the decay of fidelity in free delay, double  $\pi$ -pulses, and periodic dynamical decoupling. In the case of double  $\pi$ -pulses, essentially we set up the circuit of dynamical decoupling with only two layers of  $X$  gates separating the delay time into a 1:2:1 ratio. In the case of periodic dynamical decoupling, we put two layers of  $X$  gates for every 1  $\mu\text{s}$  of delay time, meaning that for the longest delay time of 15  $\mu\text{s}$ , there are 30 layers of  $X$  gates. In figure 3.3, we notice a significant improvement in the graph state's coherence time by evaluating its fidelity's lifetime. We assume the decay of fidelity follows a simple exponential model,

$$F(t) = F_0 \exp\left(-\frac{t}{\tau}\right), \quad (3.3)$$

where  $F_0$  is the initial fidelity before decay starts, and  $\tau$  stands for its characteristic lifetime.

After fitting the data into the function, we find that the characteristic lifetime  $\tau$  of mitigated fidelity is  $2.01 \pm 0.138\mu\text{s}$  in free delay, and  $4.20 \pm 0.367\mu\text{s}$ ,  $4.57 \pm 0.364\mu\text{s}$  for double  $\pi$ -pulses and periodic dynamical decouplings respectively, where the uncertainties take one standard error using method of least squares near the optimal curve. These values highlight the average scaling in coherence time by a factor of 2.09 and 2.27 after implementing double  $\pi$ -pulses and PDD. Based on those outcomes, we first experimentally verify the effectiveness of PDD on graph states prepared on IBM Quantum devices. Although such an entanglement preserving technique is only applied to a graph state of 5 qubits, there is no doubt that one can enforce it to large graph states as the circuit depth of each layer of  $X^{\otimes n}$ -pulses always remain unchanged.

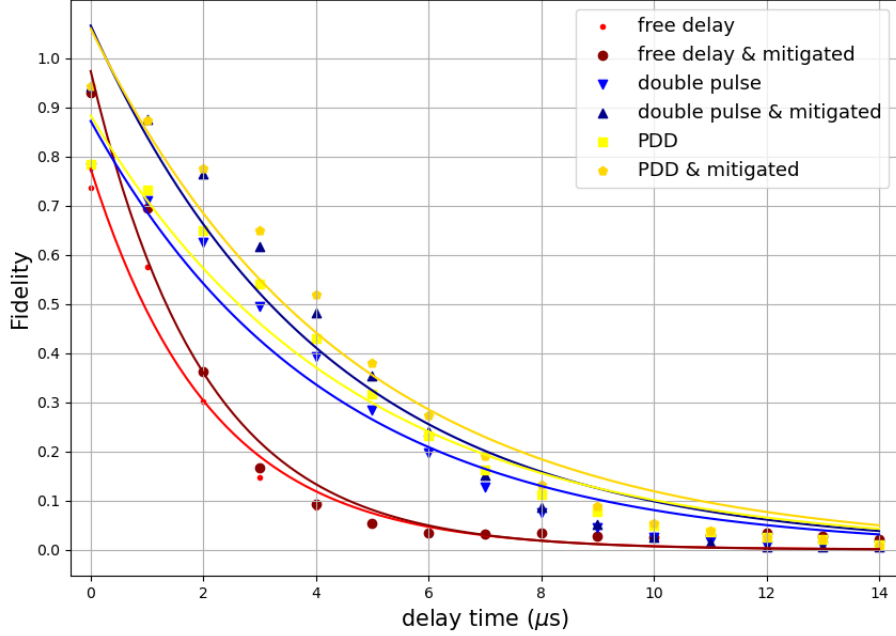


**Figure 3.3:** Decay of the fidelities of the 5-qubit graph state on *ibmq\_manila* in different entanglement preserving strategies. Red lines represent the graph state in natural delay without any interventions, whereas blue and yellow lines are with double  $\pi$ -pulses and dynamical decouplings. Mitigation indicates results processed by QREM. Both double  $\pi$ -pulses and dynamical decouplings exhibit significant improvement in fidelity over time compared to natural delays. However, only slight improvements can be observed from dynamical decoupling to double  $\pi$ -pulses.

Lastly, despite the successful demonstration of PDD, it is noticed that the average coherence time of the fidelity is still two orders of magnitude smaller than the average relaxation time  $T_1 = 154.04\mu\text{s}$  and dephasing time  $T_2 = 57.75\mu\text{s}$  of a single qubit obtained from calibration data of *ibmq\_manila*. We propose two potential explanations for this phenomenon. First, unlike measuring the de-excitation of a single-qubit state from  $|1\rangle$  to  $|0\rangle$ , fidelity is much more sensitive to perturbations in all directions and decoherence in couplings. Second, a state involving multi-qubits is naturally more fragile to environmental noises and decays faster than a single-qubit state. Therefore, we anticipate that the average lifetime should decrease even further as the graph state grows.

### 3.2.2 Outlook

As mentioned above, due to the vulnerability of the multi-qubit states subject to perturbations compared to the single-qubit state, the preservation of entanglement faces challenges when scaling into large quantum states. Thus, a possible future research direction could be enforcing other dynamical decoupling algorithms that deal with the precession errors with more degree of freedom [67, 69]. Furthermore, there are some aspects of dynamical decouplings of graph states still need to be investigated. For example, one may analyse the behaviour of negativity on decaying bipartite states discussed previously in Section 2.2 subject to dynamical decouplings.

# 4 Entanglement in Teleportation

## 4.1 Introduction

In Section 2.2, we discussed the methodologies used when characterising bipartite states entanglement that has the qubits topologically adjacent. Another important research aspect of entanglement characterisation is to measure the entanglement of bipartite states that have their qubits topologically separated by quantum teleportation. Since Bennett first proposed the method and mechanism of quantum state teleportation [70], efforts to physically realise and demonstrate quantum teleportation have been made since two decades ago. The phenomenon of quantum teleportation was first experimentally verified by Bouwmeester et al. [71] in 1997, as well as teleportation of a polarised state in [72]. As time progressed, researchers managed to perform teleportation onto distant matter-qubits [73, 74]. However, to the best of our knowledge, the quality of entanglement after multiple teleportation hops is a problem not yet been explored experimentally.

In this chapter, utilising a known measurement-based quantum computing algorithm, we characterise the entanglement of two-qubit graph states up to the local transformations that have their qubits separated at the ends of one-dimensional chains of up to 13 qubits. In our work, we impose two types of processing strategies, dynamic circuit and post-processing, where one is within the quantum circuits and the other is outside. By comparing the robustness of those strategies with the SWAP gates, where  $\text{SWAP}_{01} |\alpha\rangle_0 \otimes |\beta\rangle_1 = |\beta\rangle_0 \otimes |\alpha\rangle_1$  is a standard method of transporting quantum information, we find that the post-processing method outperforms the SWAP gates in terms of the measured negativity. Similar to previous cases, the source codes for this program are available under [https://github.com/KangHaiYue/MSc\\_Project/blob/main/main%20project/teleportation.py](https://github.com/KangHaiYue/MSc_Project/blob/main/main%20project/teleportation.py).

### 4.1.1 One-way Quantum Computation and Teleportation

In contrast to unitary quantum computation, one-way quantum computation is irreversible. Under this situation, measurement gates are inserted in the middle of a quantum circuit, resulting in a collapse of the quantum state that is not recoverable by applying a set of hermitian conjugate gates [41]. Often, the measurement results in the middle of a circuit will act as a control for applying conditional unitary gates to other qubits, which is also known as a dynamic circuit. This would allow one to manipulate the circuit during its execution by directly measuring some of its qubits at the cost of non-unitary computation. Practical hybrid algorithms can be carried out by exploiting such ‘classical logic’ embedded in quantum operations. For instance, Quantum State Teleportation [70] is a technique that transports information of a quantum state from one qubit to another using a dynamic circuit.

As demonstrated in [75] and Figure 4.1, an arbitrary quantum state  $|\varphi\rangle_{01} = U(|\alpha\rangle \otimes |\beta\rangle)$  prepared on qubit 0 and 1 is teleported along a chain of qubits that are already entangled by CZ gates on  $|+\rangle$  state. By measuring a qubit from the chain in Pauli-X basis, the information on that qubit can be teleported to one of its neighbouring qubits prepared in  $|+\rangle$  connected

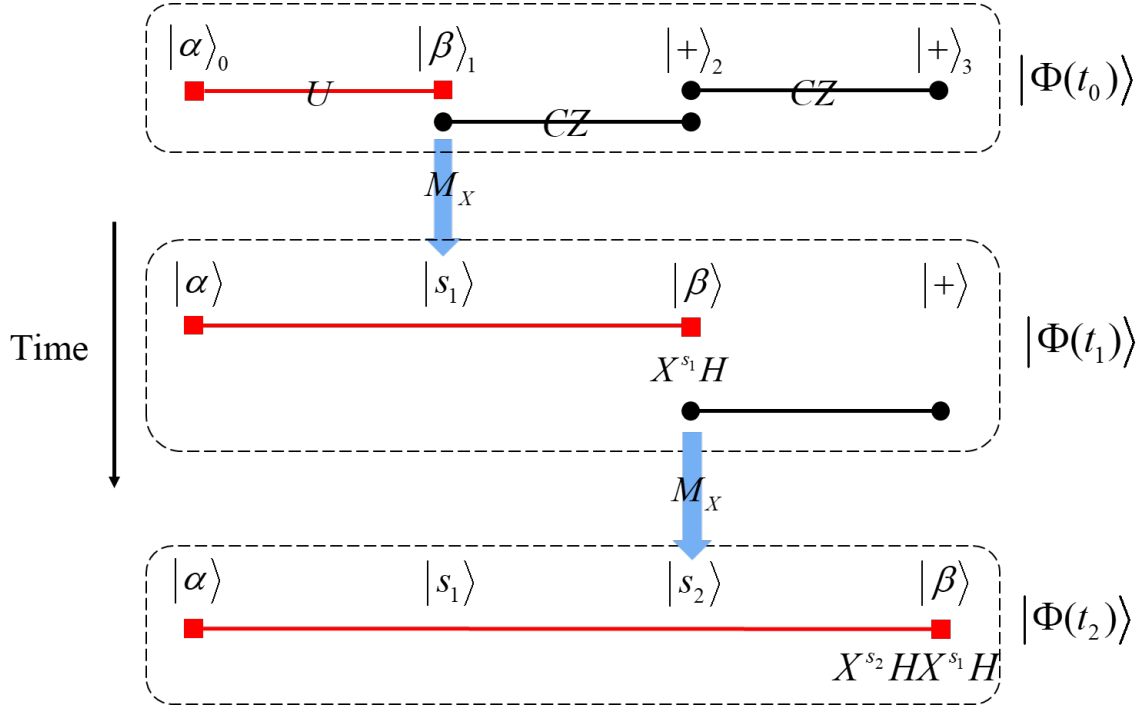


**Figure 4.1:** Demonstration of steps to teleport of the state  $|\beta\rangle$  that is already entangled with  $|\alpha\rangle$  by some arbitrary coupling gate  $U$  illustrated in orange line towards the rightmost qubit. First at  $t_0$ , initialize the two-qubit state  $|\varphi\rangle_{01} = U_{01}|\alpha\rangle_0 \otimes |\beta\rangle_1$  and entangle with Pauli-X basis eigenstates  $|+\rangle$  via  $CZ$ , producing  $|\Phi(t_0)\rangle = CZ_{23}CZ_{12}|\varphi\rangle_{01}|+\rangle_2|+\rangle_3$ ; After measuring qubit 1 in Pauli-X basis, which yield a measurement result  $|s_1\rangle$ ,  $s_1 = 0$  or  $1$ , this produce a new state  $|\Phi(t_1)\rangle = |s_1\rangle \otimes CZ_{23}(X^{s_1}H)_2|\varphi\rangle_{02}|+\rangle_3$ ; Finally, another measurement on qubit 2 yeild result  $s_2$ , leaving the teleported state at  $t_2$  to be the same state as  $U_{01}|\alpha\rangle_0|\beta\rangle_1$  up to some local transformations, namely  $|\Phi(t_2)\rangle = |s_1s_2\rangle \otimes (X^{s_2}HX^{s_1}H)_3|\varphi\rangle_{03}$

by  $CZ$ . All teleporting directions are mathematically equivalent for the case with more than one neighbouring qubits in  $|+\rangle$ . After teleportation by one hop, the original state  $|\varphi\rangle_{01}$  now rests on qubit 0 and 2 acquires some local transformation in the form of byproduct operators  $X^{s_1}H|\varphi\rangle_{02}$  [30] where  $s_1$  is the measurement result from qubit 1. More importantly, this method has a nice property: while a qubit is being teleported to a target qubit, any entanglement previously established with other qubits is preserved. This feature allows us to perform bipartite entanglement characterisation over distant qubits by teleporting state prepared on adjacent qubits. In the next section, we will verify the entanglement of graph states that have their qubits separated via teleportation along a chain of qubits prepared on graph states.

## 4.2 Teleportation of two-qubit Graph State

### 4.2.1 Dynamical circuits

Using the principle outlined above, we first design dynamical circuits to measure the negativities of the graph states after teleportation. As in Figure 4.2, we prepare graph states on a

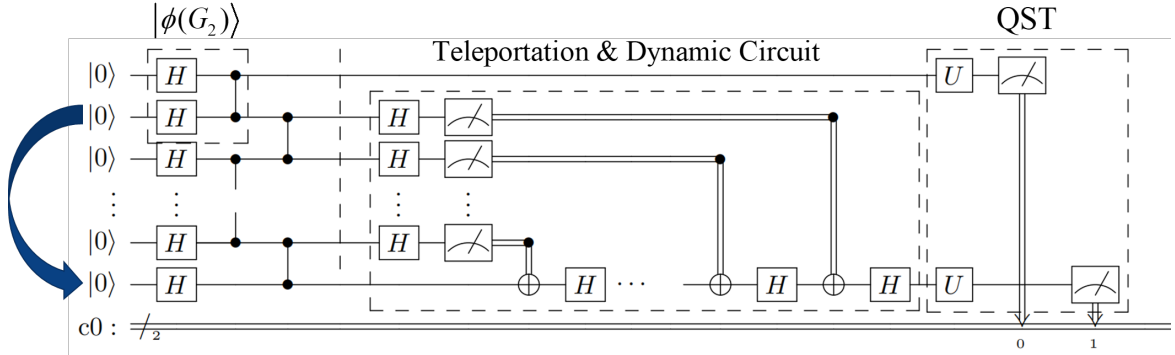


**Figure 4.2:** Illustration of the dynamic circuit for teleportation. Initially, a graph state of  $N$  qubits in a chain  $|\phi(G_N)\rangle$  is generated. The qubits in the middle are changed to Pauli- $X$  basis via Hadamards and measured. According to the measurement results, a sequence of  $X$  and Hadamard gates are conditionally applied to the last qubit to undo the local transformation. At this stage, the two-qubit graph state  $|\phi(G_2)\rangle$  originally stored in the first two qubits are now separated to the ends as indicated by the blue arrow, making the overall quantum state equal to  $|\phi(G_2)\rangle \otimes |s_1 s_2 \cdots s_{N-2}\rangle$ . Finally, QST is applied to reconstruct the density matrix of the teleported state  $|\phi(G_2)\rangle$ . The double line at the bottom represents classical registers to store measurement results.

path of  $N$  vertices so  $N$  qubits are coupled in a chain. By measuring intermediate qubits on the Pauli- $X$  basis, it teleports the information from the second qubit towards the last qubit while maintaining its entanglement with the first qubit. This is equivalent to teleporting the two-qubit graph state  $|\phi(G_2)\rangle$  from the first two qubits to the ends of the path up to local transformations. The purpose of using dynamical circuits is to undo the local transformations acting on the two-qubit graph state, where a set of conditional Pauli- $X$  and Hadamards gates are sequentially applied, and the Pauli- $X$  gates are precisely controlled by the measurement results of intermediate qubits. Lastly, QST acts on the ends of the path to reconstruct the density matrix. As in previous chapters, Algorithm 1 is also applied to find physical density matrices. A subtle point during the operations is that instead of applying *quantum* CNOT gate to the last qubit, IBM Quantum devices actively add gates *classically* determined from measurements during the circuit execution. A direct consequence is that the speed of overall circuit execution is limited by its internal classical readout/write-in speed to a large extent. Figure 4.3 shows the plot of negativity obtained from executing the circuit above on the IBM Quantum device *ibmq\_mumbai* by measuring the negativities of states teleported to positions separated by different numbers of intermediate qubits. As we gradually increase the number of teleportation hops, the average measured negativity of the two-qubit graph state teleported to the ends decreases. In our experiment, the maximal number of teleportations such that we obtain non-zero negativity after QREM is 10. If we consider the data even before any error mitigation, the figure drops down to 8. Nevertheless, this is the first time multi-hop teleportation of entangled state through intermediate nodes of graph state is achieved.

However, because of the dynamic corrections made to the teleported state, the depth of the circuits also grows linearly  $O(N)$  with respect to the number of qubits in the initial graph state. Therefore, the rapid decrease in negativity is also partially contributed by the decoherence of the state as the circuit depth increases. Therefore, this makes us unable to assess the loss of information purely caused by teleportation itself. This suggests that if one can improve the

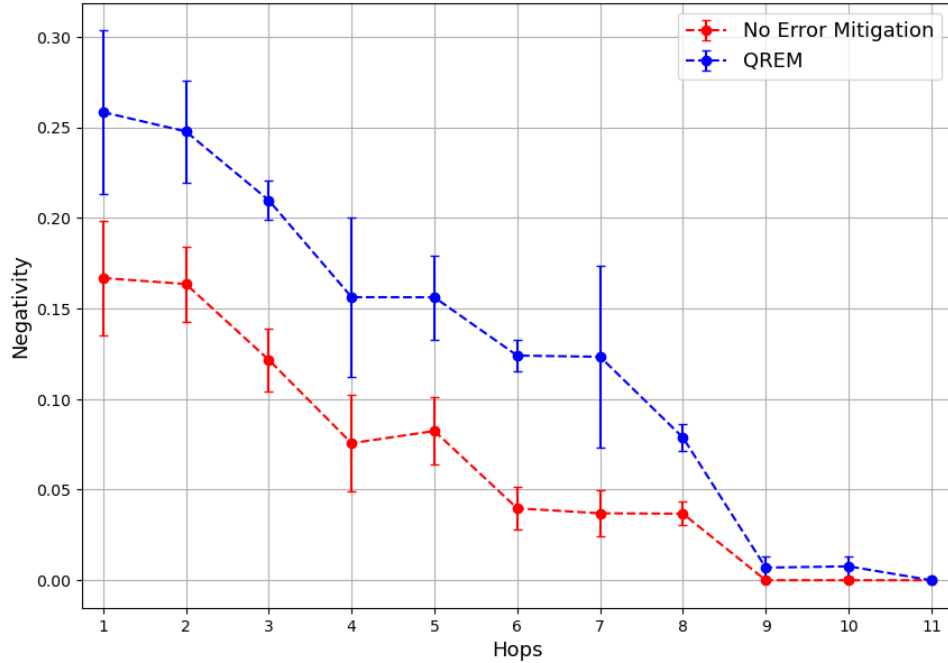


**Figure 4.3:** Plot of the negativity measured after teleporting the two-qubit graph state into different separations up to 11 intermediate qubits. Dynamic circuits are implemented as part of this calculation for undoing the local transformation after the projection of the two-qubit graph state by measuring intermediate qubits on Pauli-X bases. Due to controlled quantum operations after measuring intermediate qubits, QREM is naturally applied only to the two teleported qubits. Error bars use  $2\sigma$  of the standard error sampled in a total of 4 trials.

circuit depth for teleportation, it is reasonable to expect the maximal number of teleportation hops with non-zero negativity to increase, and the effect of state decohering due to circuit depth can be minimised. In the next section, we develop a new algorithm that reduces the growth of circuit depth for teleportation from linear order to constant with respect to the number of qubits at the cost of linear order increase in classical post-processing.

#### 4.2.2 Post-Procession of projected State

Similar to dynamic circuits, we still use the same teleportation technique to project the two-qubit graph state into separated qubits in this section. However, instead of complying with the dynamic circuit that inserts gates in a running circuit, we recognise and categorise the local transformations on the teleported state by realizing the measurement outcomes of intermediate qubits. This approach aims to tackle the problem of increasing circuit depth as the number of hops in teleportation grows. Figure 4.4 outlines the detailed procedure of the modified algorithm. By recording the measurement outcomes of the intermediate qubits but not applying undoing gates, we enforce the identification of local transformations after the circuit is completed. Therefore, the depth of the quantum circuit is now constant with respect to the number of qubits. This largely suppresses the errors due to decoherence, establishing a cleaner environment for benchmarking the loss of information caused by noise during teleportation.

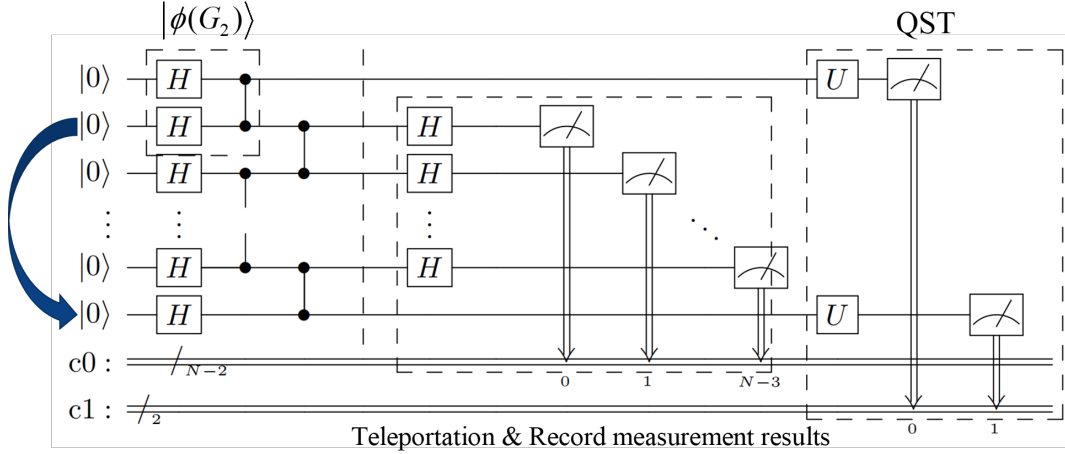


**Figure 4.4:** Illustration of the teleportation circuit without dynamic circuit. The only difference is that instead of conditionally modifying the circuit during its execution, we categorise the projected state by classical post-processing. Thus, the exact local transformations on the teleported two-qubit graph state will be identified according to the measurement outcomes stored in the classical register  $c0$  for each shot. If ignoring the measurement results of intermediate qubits, this is in an overall mixed state with pure state components of  $|\phi(G_2)\rangle^{(\vec{x},n)} \otimes |s_1 s_2 \cdots s_{N-2}\rangle$  before QST.

Furthermore, we realize that there are a constant total of eight configurations of local transformations on  $|\phi(G_2)\rangle$  depending on the number of intermediate qubits  $n$  and measurement results,

$$|\phi(G_2)\rangle^{(\vec{x},n)} = H^n \otimes I \frac{1}{2} (e^{i\pi x_1} |00\rangle + e^{i\pi x_2} |01\rangle + e^{i\pi x_3} |10\rangle + e^{i\pi x_4} |11\rangle), \quad (4.1)$$

where  $\vec{x} = (x_1, x_2, x_3, x_4)$ ,  $x_i \in \{0, 1\}$  and  $\sum_i x_i = 1$  labels one of the four possible variants of either two-qubit graph or Bell state  $|\text{Bell}\rangle = \frac{1}{\sqrt{2}}(|00\rangle + |11\rangle)$  and  $\vec{x}$  can be found by computing the transformed state analytically by applying  $X^{s_i} H$  continually to  $|\phi(G_2)\rangle$  according to the measurement result  $s_i$  of each intermediate qubit  $i$ . By massaging on the Pauli-operators, Equation 4.1 is equivalent to

$$|\phi(G_2)\rangle^{(\vec{x},n)} = H^{n-1} Z^{x_1+x_2} X^{x_1+x_3} \otimes I |\text{Bell}\rangle, \quad (4.2)$$

where  $H, X, Z$  are all acted on the same qubit. Unlike the dynamic circuits, this approach would randomly project the teleported state into one of the four variants at a fixed number of intermediate qubits. Therefore, it is impossible to reconstruct the density matrix  $\rho = |\phi(G_2)\rangle \langle \phi(G_2)|$  directly otherwise we will obtain a mixed state,

$$\rho^{(\text{mixed})} = \frac{1}{4} \sum_{\vec{x}} |\phi(G_2)\rangle^{(\vec{x},n)} \langle \phi(G_2)|^{(\vec{x},n)}. \quad (4.3)$$

Because of this, we choose to first categorise the measured outcomes into the four possible Bell state/two-qubit graph state variants before calculating their corresponding density matrices  $\rho^{(\vec{x},n)}$  respectively. Therefore, we can even omit the process of undoing local transformations  $S$  in the way of  $\rho = S^\dagger \rho' S$  since we deal with each of them separately.

Figure 4.5 demonstrates the average measured negativities on *ibmq\_mumbai* among the four configurations versus the number of hops teleported in deep-coloured lines. Similar to dynamic

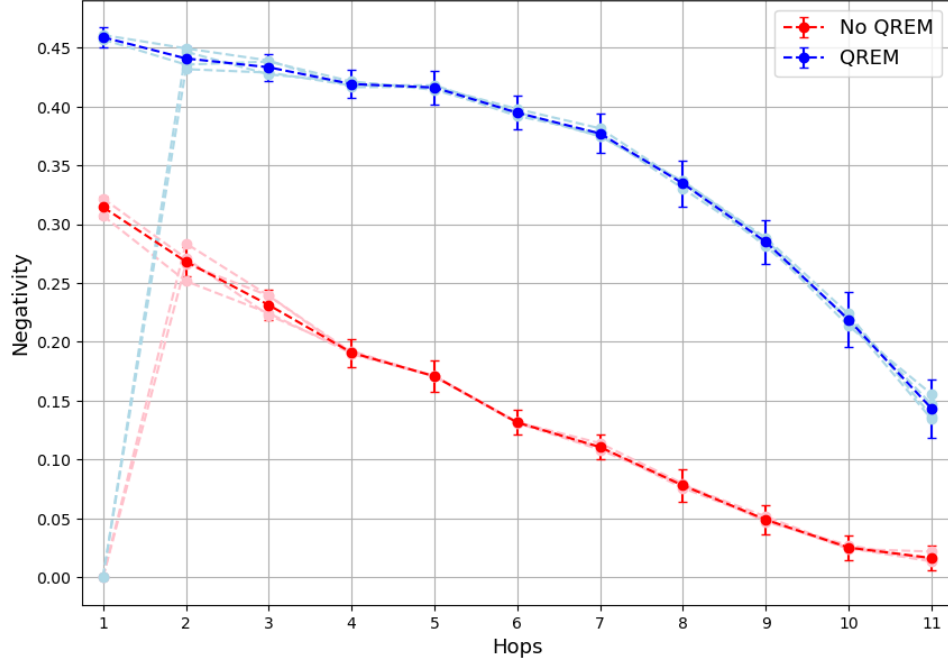


**Figure 4.5:** Plot of the negativity measured on the teleported state generated on *ibmq\_mumbai* up to 11 teleportation hoppings without dynamic circuits. Measurement results from each shot are categorised into one of the four possible configurations based on the Pauli- $X$  measurement results. Each of the light dashed lines represents one configuration, and the heavy lines are their average. N.B. that when there is just one hop, only two configurations are available, making the negativity recorded as zero for the remaining two. Error bars use  $1.96\sigma$  of the standard error sampled in a total of 4 trials.

circuits, the negativity also drops as the number of qubits hopped during teleportation increases, indicating non-perfect teleportations due to noise. However, it is also notable that the negativity decays much slower after applying QREM. Even after 11 hopped qubits where the negativity measured using a dynamic circuit already drops to zero, it still maintains a relatively high negativity reading near 0.15. This is strongly convincing to demonstrate the advantage of classical post-processing in preserving entanglement during teleportation by reducing circuit depth, as well as the advantage of being able to apply QREM to intermediate qubits as opposed to dynamic circuits. We also anticipate that the highest number of teleportation hops is not limited to 11, suggesting a direction in future research of adding more hops to teleportation until the extreme is reached.

### 4.2.3 Comparisons with the SWAP Gate Approach

Through the previous experiments, we observe the entanglement decays while the number of hops in teleportation grows. We also comment on the performance of post-processed categorisation that surpasses the intuition of dynamic circuits. In this section, we show SWAP gates as a reference method for transporting the state from the second qubit to the last as in Figure 4.6. To highlight the improvement achieved in post-processing categorisation, we quantify and compare the rates and delays of decays on all discussed approaches in Figure 4.7.

We model the negativity with respect to the number of hops as logistic decay,

$$N = \frac{N_0}{1 + \exp(\alpha n + \xi)}, \quad (4.4)$$

where  $N_0$  is the initial negativity,  $n$  is the number of hops,  $\alpha$  is the decay rate in the dimensionless unit, and  $\xi$  is the correction to the delay of decay for better estimation. After fitting the data to this curve as in Figure 4.7a, we explicitly calculate the decay rates  $\alpha$  using the least

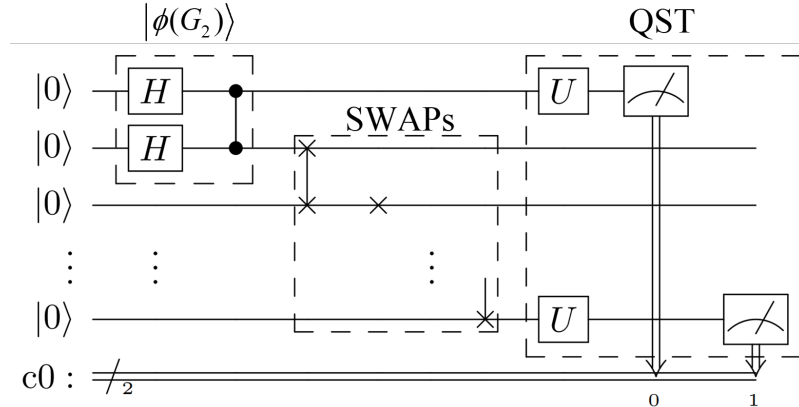


**Figure 4.6:** Circuit diagram of the simple but naive design to transport the information of the second qubit to the last by continually applying SWAP gates. Ideally, the quantum state before QST should be in the form of  $|\phi(G_2)\rangle \otimes |00\cdots 0\rangle$

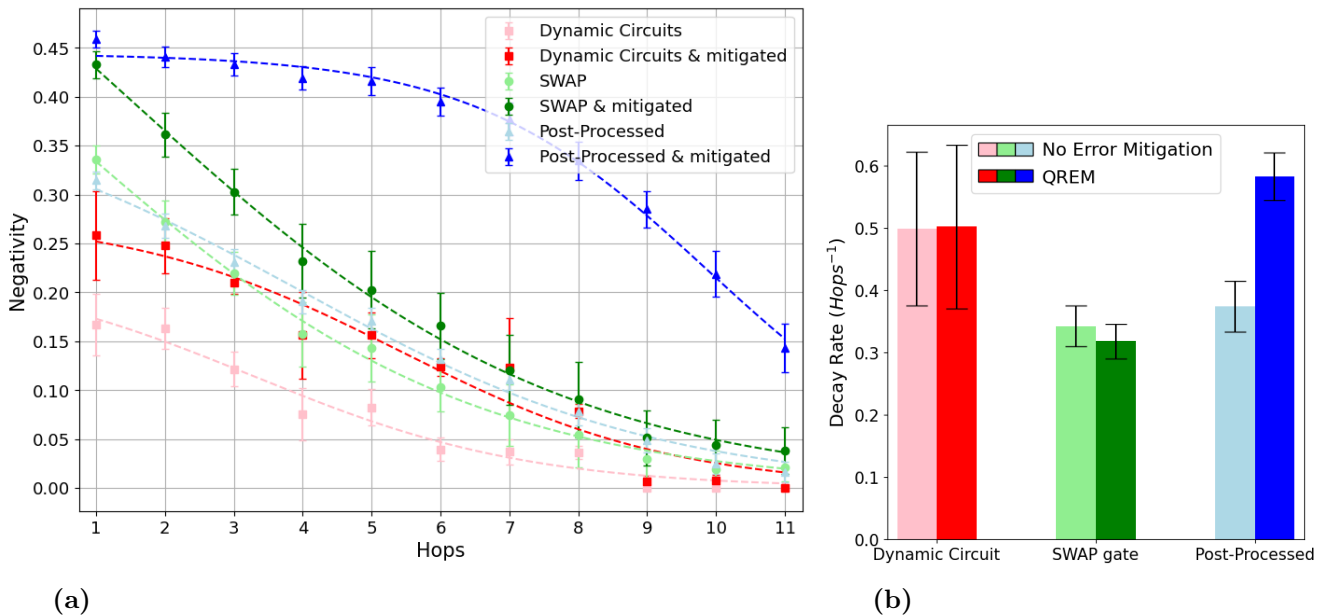


**Figure 4.7:** (a) Negativity measured using dynamic circuits, categorised/post-processed local transformations, and SWAP gates are plotted together to fit the logistic model. Light dashed lines represent the data without QREM, and heavy dashed lines are highlighted for the data after QREM. Error bars use  $1.96\sigma$  of the standard error sampled in a total of 4 trials. (b) Corresponding decay rates  $\alpha$  of each approach, error bars representing the standard error of the parameter. N.B. that the high decay rate of the post-processed method is compensated by its large delay of decay  $\xi$ .

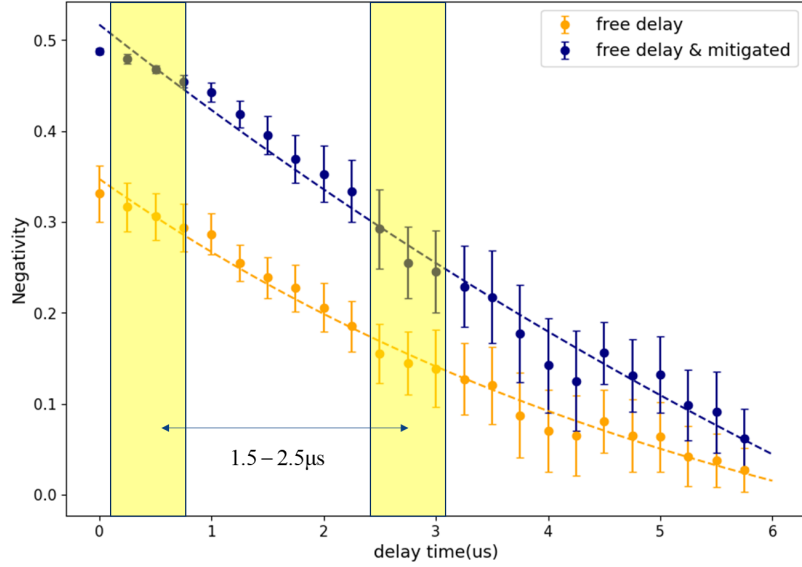


**Figure 4.8:** Plot of the average two-qubit graph state negativity both with and without QREM versus delay time on the IBM Quantum device *ibmq\_mumbai*. The average time for the negativity to decay from near 0.464 and 0.314 (teleportation by once using post-processed categorisation with and without QREM, marked by the first band) to near 0.264 and 0.167 (teleportation by one hop using dynamic circuits with and without QREM, marked by the second band) is roughly 1.5 $\mu$ s to 2.5 $\mu$ s.

residual squares method and compare them in Figure 4.7b. Although the **decay rate** from the method of post-processing is higher than the method SWAP gates ( $0.583 \pm 0.0385$  hop $^{-1}$  versus  $0.315 \pm 0.0278$  hop $^{-1}$  after QREM), overall the remaining entanglement is much higher, which is explained by the large improvement in the **delay of decay**  $\xi$  on post-processed categorisation compares to SWAP gates ( $5.76 \pm 0.387$  versus  $0.456 \pm 0.384$ ) that overcome the previous disadvantage. The quick drop of the negativity in the blue curve at the end could be a result of particularly poorly performing intermediate qubit(s) when mitigating its readout error. Such behaviour is not observed in other methods since only the two ending qubits are mitigated. Overall, the fast decoherence of the graph state during teleportation using SWAP gates is likely caused by the large circuit depth that grows linearly with respect to the number of hops and contributes three CNOTs for every SWAP gate. At the same time, we note that while preserving a relatively high amount of entanglement, the classical categorisation after teleportation also does not rely on quantum interactions to transmit messages like SWAP gates.

Meanwhile, we also recognise that there is a considerable gap of 0.147 and 0.201 in negativity before and after QREM, even after just one hop using dynamic circuits and post-processed categorisation. Yet, the dynamic circuit's depth is only increased by at most two. We interpret this as the long gate execution time of the dynamic CNOT gate, such that even just one hop can cause a significant delay in the circuit. To quantify this, we measure the average negativity of the two-qubit graph state experiencing a delay on the same machine in Figure 4.8. The time it takes for the negativity to reduce by the amount indicated above (0.147 before QREM, 0.201 after QREM) is roughly 1.5–2.5 $\mu$ s. Supposing this is the effective gate time of the dynamical equivalent to a CNOT gate, it is indeed much longer than the typical quantum CNOT gate time, which is in the range of 200 – 700ns. Therefore, it suggests that longer gate times could be a significant contributor to the reduction in negativity.

# 5 Conclusion and Outlook

In the current field of entanglement characterisation, many algorithms are developed to verify, evaluate, and preserve quantum states efficiently. However, many lack scalability or have yet to be physically demonstrated for large quantum states. Such a situation limits the benchmarking of real quantum devices, especially those that can map large entangled states. To fill this gap, this thesis examines existing algorithms for large states on IBM Quantum devices and presents new candidates that are better optimised in their scalability and accuracy.

In Chapter 1, by conducting a Literature Review, We first introduced the fundamental concepts of quantum computation, entanglement, technical routes in quantum computers, and their limitations to readers. We also discussed basic entanglement characterisation metrics, including quantum state tomography, negativity, fidelity, and standard error mitigation techniques such as QREM. This presented a thorough summary of the application of entanglement characterisation in the noisy intermediate-scale quantum (NISQ) era, as well as the primary concern of this work to benchmark the quality of entanglement on near-term NISQ quantum devices.

In Chapter 2, we characterised entanglement on graph states. We demonstrated non-zero negativities of all nearest-neighbour Bell states projected from a record-breaking 414-qubit graph state. We verified the credibility of QREM by confirming that it was not over-correcting the negativities over its theoretical values after scanning through different  $CZ$  rotation angles. Utilising the randomised stabilisers on Fidelity Estimation, we generated graph states that are GME up to 14 qubits by measuring the fidelity of  $0.58 \pm 0.06$  within limited resources. Furthermore, we developed a new strategy for characterising entanglement by measuring a state's energy using Hamiltonian moments. By showing only logarithmic growth in the number of circuits with respect to the number of qubits, we highlighted its extreme friendliness in time-cost and demonstrated a measure of entanglement on graph states up to 127-qubit with  $E_0 = -0.812 \pm 0.007$ . We also observed the trend of graph states moving close to Hamiltonian eigenstates as the number of qubits increased by comparing the ratio of the first moment to corrected energy  $c_1/E_0$ .

In Chapter 3, we verified periodic dynamical decoupling as an entanglement preserving strategy on graph state prepared on an IBM superconducting quantum device, which was not done previously. Despite challenges in scaling up to a larger entangled state, we still observed a doubling in the characteristic lifetime of  $4.57 \pm 0.364\mu\text{s}$  by measuring the fidelities of a 5-qubit graph state prepared on *ibmq\_manila*.

In Chapter 4, established from the theory of one-way quantum computation, we developed new approaches to entanglement teleportation. By measuring the negativities of the teleported two-qubit graph states using dynamical circuits, post-processed categorisation, and non-teleporting SWAP gates respectively, we showed that the method of post-processed categorisation outperformed the others in terms of minimising information lost during teleportation hops. Under this approach, we sustained entanglement after teleporting across 11 qubits.

Overall, this work optimised tools available for verifying, preserving, and teleporting entanglement by providing more scalable algorithms. We enforced those algorithms on recent IBM Quantum devices and successfully benchmarked their capabilities in preparing large-entangled states.

Beyond the studies in this work, we propose possible future research topics based on the current outcomes.

- **Characterisation of non-nearest neighbour bipartite entanglement:** Study on the characterisation of bipartite entanglement between qubits that are not the nearest neighbour potentially offers another scalable method of measuring entanglement on large graph states. Quantum teleportation can play an important role in answering such a question.
- **Establishing relationship between energies to fidelities:** Further investigate the relationship between energies measured using Hamiltonian moments to the state fidelities, preferably establishing rigorous mathematical proofs on the lower and upper bounds of the energies with respect to specific states under the perturbation of noises.
- **Optimised Dynamical Decoupling:** Further explores other dynamical decoupling strategies on graph states that consider more degrees of freedom than just  $X$ -axis. In principle, this should further optimise the coherence time/lifetime of any prepared state. Possible methodologies may include concatenated dynamical decoupling (CDD) [67] and Uhrig dynamical decoupling (UDD) [76].
- **Randomised Fidelity Estimation on other entangled states:** Compares the efficiency and effectiveness of fidelity estimation using randomised stabilisers on other stabiliser states, hence examining the universality of such technique in characterising entanglement.

# Bibliography

- <sup>1</sup>R. P. Feynman, “Simulating physics with computers”, in *Feynman and computation* (CRC Press, 2018), pp. 133–153.
- <sup>2</sup>P. Shor, “Algorithms for quantum computation: discrete logarithms and factoring”, in *Proceedings 35th Annual Symposium on Foundations of Computer Science* (1994), pp. 124–134.
- <sup>3</sup>L. K. Grover, *A fast quantum mechanical algorithm for database search*, 1996.
- <sup>4</sup>A. Peruzzo *et al.*, “A variational eigenvalue solver on a photonic quantum processor”, *Nature Communications* **5**, 10.1038/ncomms5213 (2014).
- <sup>5</sup>E. Farhi, J. Goldstone, and S. Gutmann, “A quantum approximate optimization algorithm”, *arXiv preprint arXiv:1411.4028* (2014).
- <sup>6</sup>J. Biamonte *et al.*, “Quantum machine learning”, *Nature* **549**, 195–202 (2017).
- <sup>7</sup>S. McArdle *et al.*, “Quantum computational chemistry”, *Reviews of Modern Physics* **92**, 10.1103/revmodphys.92.015003 (2020).
- <sup>8</sup>M. Schuld, I. Sinayskiy, and F. Petruccione, “An introduction to quantum machine learning”, *Contemporary Physics* **56**, 10.1080/00107514.2014.964942 (2014).
- <sup>9</sup>L. C. L. Hollenberg, “Fast quantum search algorithms in protein sequence comparisons: Quantum bioinformatics”, *Phys. Rev. E* **62**, 7532–7535 (2000).
- <sup>10</sup>O. Román, M. Samuel, and L. Enrique, “Quantum Computing for Finance: Overview and Prospects”, *Reviews in Physics* **4** (2019).
- <sup>11</sup>E. Rieffel and W. Polak, “An introduction to quantum computing for non-physicists”, *ACM Computing Surveys (CSUR)* **32**, 300–335 (2000).
- <sup>12</sup>A. Einstein, B. Podolsky, and N. Rosen, “Can Quantum-Mechanical Description of Physical Reality Be Considered Complete?”, *Phys. Rev.* **47**, 777–780 (1935).
- <sup>13</sup>J. S. Bell, “On the Einstein Podolsky Rosen paradox”, *Physics Physique Fizika* **1**, 195–200 (1964).
- <sup>14</sup>S. J. Freedman and J. F. Clauser, “Experimental Test of Local Hidden-Variable Theories”, *Phys. Rev. Lett.* **28**, 938–941 (1972).
- <sup>15</sup>G. J. Mooney, C. D. Hill, and L. C. L. Hollenberg, “Entanglement in a 20-Qubit Superconducting Quantum Computer”, *Scientific Reports* **9**, 10.1038/s41598-019-49805-7 (2019).
- <sup>16</sup>M. A. Nielsen and I. L. Chuang, *Quantum Computation and Quantum Information* (Cambridge University Press, 2022).
- <sup>17</sup>C. D. Bruzewicz *et al.*, “Trapped-ion quantum computing: Progress and challenges”, *Applied Physics Reviews* **6**, 10.1063/1.5088164 (2019).
- <sup>18</sup>J. L. O’Brien, “Optical Quantum Computing”, *Science* **318**, 1567–1570 (2007).
- <sup>19</sup>L. Childress and R. Hanson, “Diamond NV centers for quantum computing and quantum networks”, *MRS bulletin* **38**, 134–138 (2013).
- <sup>20</sup>L. Hollenberg *et al.*, “Charge-based quantum computing using single donors in semiconductors”, *Physical Review B* **69**, 113301 (2004).
- <sup>21</sup>F. Arute *et al.*, “Quantum supremacy using a programmable superconducting processor”, *Nature* **574**, 505–510 (2019).
- <sup>22</sup>“IBM Unveils 400 Qubit-Plus Quantum Processor and Next-Generation IBM Quantum System Two”, *IBM Newsroom* (2022).
- <sup>23</sup>E. Gibney, “Hello quantum world! Google publishes landmark quantum supremacy claim”, *Nature* (2019).
- <sup>24</sup>S. Cao *et al.*, “Generation of genuine entanglement up to 51 superconducting qubits”, *Nature*, 1–5 (2023).
- <sup>25</sup>C. Gidney and M. Ekerå, “How to factor 2048 bit RSA integers in 8 hours using 20 million noisy qubits”, *Quantum* **5**, 433 (2021).

- <sup>26</sup>Morrison and Ryan, “Quantinuum H-Series quantum computer accelerates through 3 more performance records for quantum volume:  $2^{17}$ ,  $2^{18}$ , and  $2^{19}$ ”, ([2023-6-30](#)).
- <sup>27</sup>R. Acharya *et al.*, “Suppressing quantum errors by scaling a surface code logical qubit”,
- <sup>28</sup>Y. Zhao *et al.*, “Realization of an Error Correcting Surface Code with Superconducting Qubits”, *Physical Review Letters* **129**, 10.1103/physrevlett.129.030501 (2022).
- <sup>29</sup>S. Krinner *et al.*, “Realizing repeated quantum error correction in a distance-three surface code”, *Nature* **605**, 669–674 (2022).
- <sup>30</sup>A. G. Fowler *et al.*, “Surface codes: Towards practical large-scale quantum computation”, *Physical Review A* **86**, 10.1103/physreva.86.032324 (2012).
- <sup>31</sup>J. Preskill, “Quantum Computing in the NISQ era and beyond”, *Quantum* **2**, 79 (2018).
- <sup>32</sup>J. F. Kam *et al.*, “Paper in preparation”,
- <sup>33</sup>G. J. Mooney *et al.*, “Whole-Device Entanglement in a 65-Qubit Superconducting Quantum Computer”, *Advanced Quantum Technologies* **4**, 2100061 (2021).
- <sup>34</sup>C. Song *et al.*, “Generation of multicomponent atomic Schrödinger cat states of up to 20 qubits”, *Science* **365**, 574–577 (2019).
- <sup>35</sup>S. A. Moses *et al.*, *A Race Track Trapped-Ion Quantum Processor*, 2023.
- <sup>36</sup>A. Wack *et al.*, “Quality, speed, and scale: three key attributes to measure the performance of near-term quantum computers”, *arXiv preprint arXiv:2110.14108* (2021).
- <sup>37</sup>D. Z. Petar Jurcevic, I. L. Jiri Stehlík, and R. Mandelbaum, “Pushing quantum performance forward with our highest Quantum Volume yet”, *IBM Research Blog* (2022).
- <sup>38</sup>R. Harper, S. T. Flammia, and J. J. Wallman, “Efficient learning of quantum noise”, *Nature Physics* **16**, 1184–1188 (2020).
- <sup>39</sup>M. Hein, J. Eisert, and H. J. Briegel, “Multiparty entanglement in graph states”, *Phys. Rev. A* **69**, 062311 (2004).
- <sup>40</sup>H. J. Briegel and R. Raussendorf, “Persistent Entanglement in Arrays of Interacting Particles”, *Phys. Rev. Lett.* **86**, 910–913 (2001).
- <sup>41</sup>R. Raussendorf, D. E. Browne, and H. J. Briegel, “Measurement-based quantum computation on cluster states”, *Physical Review A* **68**, 10.1103/physreva.68.022312 (2003).
- <sup>42</sup>M. Hein *et al.*, *Entanglement in Graph States and its Applications*, 2006.
- <sup>43</sup>B. M. Terhal, “Bell inequalities and the separability criterion”, *Physics Letters A* **271**, 319–326 (2000).
- <sup>44</sup>S. T. Flammia and Y.-K. Liu, “Direct fidelity estimation from few Pauli measurements”, *Physical review letters* **106**, 230501 (2011).
- <sup>45</sup>G. Vidal and R. F. Werner, “Computable measure of entanglement”, *Phys. Rev. A* **65**, 032314 (2002).
- <sup>46</sup>H. Shapourian, K. Shiozaki, and S. Ryu, “Partial time-reversal transformation and entanglement negativity in fermionic systems”, *Physical Review B* **95**, 165101 (2017).
- <sup>47</sup>G. J. Mooney *et al.*, “Generation and verification of 27-qubit Greenberger-Horne-Zeilinger states in a superconducting quantum computer”, *Journal of Physics Communications* **5**, 095004 (2021).
- <sup>48</sup>P. D. Nation *et al.*, “Scalable Mitigation of Measurement Errors on Quantum Computers”, *PRX Quantum* **2**, 040326 (2021).
- <sup>49</sup>J. A. Smolin, J. M. Gambetta, and G. Smith, “Efficient Method for Computing the Maximum-Likelihood Quantum State from Measurements with Additive Gaussian Noise”, *Phys. Rev. Lett.* **108**, 070502 (2012).
- <sup>50</sup>C. Michelot, “A finite algorithm for finding the projection of a point onto the canonical simplex of  $\mathbb{R}^n$ ”, *Journal of Optimization Theory and Applications* **50**, 195–200 (1986).

- <sup>51</sup>H. J. Vallury *et al.*, “Quantum computed moments correction to variational estimates”, *Quantum* **4**, 373 (2020).
- <sup>52</sup>M. Steffen *et al.*, “A new Eagle in the Poughkeepsie Quantum Datacenter: IBM Quantum’s most performant system yet”, *IBM Research Blog* (2022).
- <sup>53</sup>I. Pogorelov *et al.*, “Compact Ion-Trap Quantum Computing Demonstrator”, *PRX Quantum* **2**, 020343 (2021).
- <sup>54</sup>L. C. L. Hollenberg, “Plaquette expansion in lattice Hamiltonian models”, *Phys. Rev. D* **47**, 1640–1644 (1993).
- <sup>55</sup>C. Lanczos, “An iteration method for the solution of the eigenvalue problem of linear differential and integral operators”, (1950).
- <sup>56</sup>F. C. et al., “Paper in preparation”,
- <sup>57</sup>J. Cotler and F. Wilczek, “Quantum Overlapping Tomography”, *Phys. Rev. Lett.* **124**, 100401 (2020).
- <sup>58</sup>D. Gross *et al.*, “Quantum State Tomography via Compressed Sensing”, *Phys. Rev. Lett.* **105**, 150401 (2010).
- <sup>59</sup>M. Cramer *et al.*, “Efficient quantum state tomography”, *Nature Communications* **1**, 10.1038/ncomms1147 (2010).
- <sup>60</sup>G. Torlai *et al.*, “Neural-network Quantum State Tomography”, *Nature Physics* **14**, 447–450 (2018).
- <sup>61</sup>J.-C. Régin, M. Rezgui, and A. Malapert, “Embarrassingly Parallel Search”, in *Principles and Practice of Constraint Programming* (2013), pp. 596–610.
- <sup>62</sup>D. N. Jamieson *et al.*, “Deterministic atom placement by ion implantation: Few and single atom devices for quantum computer technology”, in *2016 21st International Conference on Ion Implantation Technology (IIT)* (IEEE).
- <sup>63</sup>L. Chirolli and G. Burkard, “Decoherence in solid-state qubits”, *Advances in Physics* **57**, 225–285 (2008).
- <sup>64</sup>R. Savytskyy *et al.*, “An electrically driven single-atom “flip-flop” qubit”, *Science Advances* **9**, eadd9408 (2023).
- <sup>65</sup>J. A. Schreier *et al.*, “Suppressing charge noise decoherence in superconducting charge qubits”, *Phys. Rev. B* **77**, 180502 (2008).
- <sup>66</sup>L. Viola and S. Lloyd, “Dynamical suppression of decoherence in two-state quantum systems”, *Phys. Rev. A* **58**, 2733–2744 (1998).
- <sup>67</sup>K. Khodjasteh and D. A. Lidar, “Fault-Tolerant Quantum Dynamical Decoupling”, *Physical Review Letters* **95**, 10.1103/physrevlett.95.180501 (2005).
- <sup>68</sup>E. L. Hahn, “Spin Echoes”, *Phys. Rev.* **80**, 580–594 (1950).
- <sup>69</sup>G. S. Uhrig, “Keeping a Quantum Bit Alive by Optimized  $\pi$ -Pulse Sequences”, *Phys. Rev. Lett.* **98**, 100504 (2007).
- <sup>70</sup>C. H. Bennett *et al.*, “Teleporting an unknown quantum state via dual classical and Einstein-Podolsky-Rosen channels”, *Phys. Rev. Lett.* **70**, 1895–1899 (1993).
- <sup>71</sup>D. Bouwmeester *et al.*, “Experimental quantum teleportation”, *Nature* **390**, 575–579 (1997).
- <sup>72</sup>Y.-H. Kim, S. P. Kulik, and Y. Shih, “Quantum Teleportation of a Polarization State with a Complete Bell State Measurement”, *Phys. Rev. Lett.* **86**, 1370–1373 (2001).
- <sup>73</sup>S. Olmschenk *et al.*, “Quantum teleportation between distant matter qubits”, *Science* **323**, 486–489 (2009).
- <sup>74</sup>S. Hermans *et al.*, “Qubit teleportation between non-neighbouring nodes in a quantum network”, *Nature* **605**, 663–668 (2022).
- <sup>75</sup>R. Jozsa, *An introduction to measurement based quantum computation*, 2005.
- <sup>76</sup>M. J. Biercuk *et al.*, “Experimental Uhrig dynamical decoupling using trapped ions”, *Physical Review A* **79**, 10.1103/physreva.79.062324 (2009).